ISTITUTO NAZIONALE DI FISICA NUCLEARE
Sezione di Genova

INFN/AE-01/04
6th April 2001

Study report on the *EUSO* photo-detector design

M. Ameri[(a)], S. Cuneo[(a)], F. Fontanelli[(a,b)], V. Gracco[(a,b)], P. Musico[(a)], M. Pallavicini[(a)], A. Petrolini[(*,a,b)], F. Pratolongo[(a)] and M. Sannino[(a,b)]
[(a)] *INFN, Sezione di Genova, Via Dodecaneso 33, Genova, Italy*
[(b)] *Dipartimento di Fisica dell'Università di Genova, Via Dodecaneso 33, Genova, Italy*

Abstract

The aim of this report is to summarize the $R\&D$ and the work done so far for the design of a photo-detector for a space experiment based on the AirWatch concept, focusing on the *EUSO* project proposed to ESA for installation on the International Space Station. The main results will be summarized, solutions to some problems will be presented and the most critical items requiring further study will be identified. A realistic baseline scheme for the photo-detector, based on the presently known information and constraints, is proposed. The outcome of these studies can be used to estimate the performance of *EUSO* and to provide input to further engineering studies. Finally an activity plan for the development of the photo-detector will be presented.

(*) Corresponding author. e-mail: Alessandro.Petrolini@ge.infn.it

Published by **SIS-Pubblicazioni**
Laboratori Nazionali di Frascati

Contents

Chapter 1

The *EUSO* experiment

1.1 The scientific issues

The origin of the very high-energy cosmic rays ($E > 10^{20}$ eV) is one of the most interesting and controversial problems of high-energy Astrophysics. The discovery of cosmic rays with such a large energy (Extreme Energy Cosmic Rays, EHECR) opened a new chapter in the Astrophysical Sciences, both from the observational point of view and from the theoretical one.

These cosmic rays can be observed by means of the giant showers which they produce interacting with the Earth atmosphere. About twenty events with an energy larger than $\approx 10^{20}$ eV have been observed so far. This high-energy is above the maximum energy allowed by the interaction with the cosmic background radiation over cosmological distances for all known particles, except neutrinos.

The commissioning of detectors of giant atmospheric showers, in order to increase the number of observed very high energy cosmic rays, would help to shed light on the mystery of their origin, on the accelerating mechanism on their propagation through space and on the extension to very high energies of the cosmic rays spectrum.

Very high-energy cosmic rays reach the Earth with a low flux and sophisticated and complex detectors are therefore required to study them. Some projects, based on international collaborations, are under study and definition in all the world, both for the observation from the Earth (project Auger) and for the observation from space (project *EUSO*).

The observational technique which has been chosen as the most promising one consists in the detection of the nitrogen fluorescence light produced by the particles showering in the Earth atmosphere as well as the diffuse reflection of the Cherenkov light at the Earth surface. The fluorescence emission, directly related to the number of charged particles in the shower, allows to determine the shower evolution in the atmosphere, to measure its energy and to determine the direction of the primary cosmic ray. In this approach the at-

mosphere is at the same time absorber of the incident particle and signal generator.

The detector must be equipped with an optical system with a large field of view to be able to observe a mass of atmosphere as large as possible. It must have a good sensitivity to be able to detect the faint signal from the less energetic showers, allowing to connect the observed energy spectrum with the observations from the previous experiments at lower energy. The required information can nevertheless be obtained with a system having only a limited spatial resolution. With a sufficiently fast detector it is possible to determine the direction of the primary cosmic ray without the need for a stereo view, that is with only one observatory. This observation can be done from the Earth surface, but a better sensitivity can be obtained by observing from space as a larger mass of the atmosphere can be observed and therefore a larger number of events is expected.

The big technological difficulties of such a project require a vigorous program of research and development.

1.2 The *EUSO* project

EUSO (Extreme Universe Space Observatory) was proposed to ESA, on January 2000, in answer to the announcement of opportunity for the F2/F3 missions. The experiment is dedicated to the investigation of the Extreme Energy particles present in the cosmic radiation.

It was originally proposed as an experimental apparatus for a free-flyer satellite. *EUSO* has been approved by ESA, in March 2000, for an accommodation study on board of the International Space Station (ISS).

The accommodation study on the ISS was submitted to ESA on December 2000. The final ESA answer is expected by March 2001. A positive answer will allow to start a full phase A study, that is the phase dedicated to the detailed study and design of the experiment.

An artist view of the *EUSO* payload for the ISS is shown in figure 1.1.

1.3 *EUSO* scientific objectives

EUSO was designed to look for very high-energy cosmic rays with $E \gtrsim 10^{19}$ eV (EHECR) producing Extensive Air Showers (EAS) in the atmosphere.

The following design goals were proposed.

- EHECR detection: $\approx 10^3$ events per year with $E > 10^{20}$ eV. Determination of the spectrum, arrival directions (angular distribution, clustering) with a threshold of $\approx 4 \cdot 10^{19}$ eV.

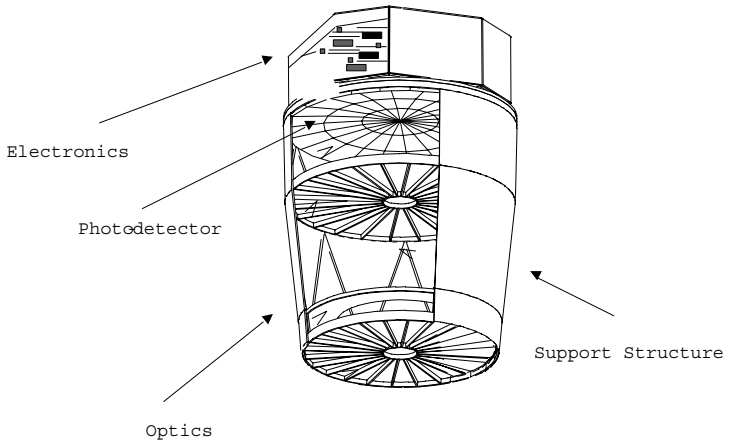

Figure 1.1: An artist view of the *EUSO* payload for the ISS [4].

- Neutrino induced EAS (the rate strongly depends on the models). Overall expected detection rate up to $\approx 10^2$ per year with $E \gtrsim 4{\cdot}10^{19}$ eV.
- Atmospheric physics.

1.4 *EUSO* parameters

The present provisional *EUSO* parameters [2,3,1,4], the ones most relevant to the photo-detector design, are summarized in table 1.4.

The approximate relations used to estimate the relevant photo-detector parameters are summarized in this section. The relations in this section will be essentially geometrical, more refined estimates will be proposed in the rest of the report.

The characteristics of the optics have a strong impact on the photo-detector design. The Point Spread Function (PSF) of the optics has to match, approximately, the photo-detector pixel size. The focal surface shape and dimensions are determined by the optics. At this stage, therefore, only rough estimates of the corresponding photo-detector parameters will be attempted. A more careful evaluation will be carried on once the design of the optics will be better defined.

The desired number of pixels of the photo-detector can be estimated, from the desired parameters, by the relation

$$N \approx \frac{\pi H^2 \tan^2 \gamma}{\Delta^2} \quad . \tag{1.1}$$

The required photo-detector pixel size, δ, corresponding to observing a length Δ on

General	
Desired pixel size at the Earth surface	$\Delta \approx 0.8\ \mathrm{km}$
ISS average orbit height	$H \simeq 380\ \mathrm{km}$
Overall atmospheric transmission ($330\ \mathrm{nm} \leq \lambda \leq 400\ \mathrm{nm}$)	$K_{atm} \simeq 0.4$
Background ($330\ \mathrm{nm} \leq \lambda \leq 400\ \mathrm{nm}$ at $\approx 400\ \mathrm{km}$ height)	$B \approx 3 \cdot 10^{11}$ photons $\cdot\ \mathrm{m}^{-2}\mathrm{s}^{-1}\mathrm{str}^{-1}$
Observation duty cycle	$\eta \simeq 0.1 \div 0.2$
Orbital period	$T_0 \simeq 90$ min
Optics [5]	
Optics maximum diameter	$D_M = 2.5\ \mathrm{m}$
Optics aperture (entrance pupil diameter)	$D = 2\ \mathrm{m}$
Optics $f\#$	$f\# = 1.25$
Optics field of view (half-angle)	$FOV = 30^\circ \equiv \gamma$
Average transmission of the optics	$K_{opt} \simeq 0.5$
Photo-detector	
Geometry of the focal surface	spherical, radius $= Df\# = 2.5\ \mathrm{m}$
Angular aperture of the focal surface	$\beta \simeq 30^\circ$
Overall photo-detector efficiency	$\varepsilon_{det} \simeq 0.15$

Table 1.1: Assumed AirWatch/*EUSO* parameters (for the ISS).

the Earth surface, can be estimated by the relation

$$\delta \approx \frac{f\Delta}{H} \quad , \tag{1.2}$$

where f is the focal length of the optics.

The photo-detector surface has to approximate the focal surface of the optics. The latter is assumed to have a spherical shape with radius equal to the focal length of the optics [5], f, and maximum angular aperture β. Its area is then given by the relation

$$A_{det} = 2\pi f^2 \left[1 - \cos\beta\right] \quad . \tag{1.3}$$

The focal surface maximum diameter is given by

$$D_f = 2f \sin\beta \quad . \tag{1.4}$$

Note that, at least to a first approximation, $\beta \simeq \gamma$.

The approximate maximum number of pixels which can be fitted on the focal surface of the photo-detector is given by the relation

$$n \approx \frac{A_{det}}{\delta^2} \quad . \tag{1.5}$$

Alternatively the desired pixel dimension on the focal surface can be estimated, in terms of the focal surface parameters and the desired number of pixels one wants to see at

the Earth, by the relation

$$d \approx \sqrt{\frac{A_{det}}{N}} \quad . \tag{1.6}$$

Note that, to the present level of approximation and with the present parameters, the two relations 1.2 and 1.6 are roughly equivalent, given the relations 1.1 and 1.3.

The optics also determines the distribution of incidence angles of the photons on the focal surface, which has some impact on the photo-detector design. The marginal ray angle is determined by the $f\#$ of the optics and is given by the relation

$$\tan\theta_{max} \approx \frac{1}{2f\#} \quad . \tag{1.7}$$

The angular sensitivity of the photo-detector, $\Delta\alpha$, is given by the relations

$$\Delta\alpha \approx \frac{\Delta}{H} \simeq \frac{\delta}{f} \quad . \tag{1.8}$$

The solid angle coverage of every pixel, $\Delta\Omega$, is given by

$$\Delta\Omega \approx \frac{\Delta^2}{H^2} \simeq \frac{\delta^2}{f^2} \simeq [\Delta\alpha]^2 \quad . \tag{1.9}$$

The approximate defocusing in the direction parallel to the focal surface, Δw, produced by a small displacement Δz in the direction perpendicular to the focal surface, is given by the relation

$$\Delta w \approx \Delta z \tan\theta_{max} = \frac{\Delta z}{2f\#} \quad . \tag{1.10}$$

The relevant *EUSO* parameters, derived from the previous assumptions and formulae, are listed in table 1.4.

Focal surface maximum diameter	2.50 m
Focal surface area	5.26 m^2
Area of the entrance pupil	3.14 m^2
Angle of the marginal ray	$21.8°$
Desired number of channels	$N = 2.36 \cdot 10^5$
Maximum number of channels fitting on the focal surface	$n = 1.90 \cdot 10^5$
Required pixel size on the focal surface	$d = 4.72$ mm

Table 1.2: AirWatch/*EUSO* parameters (for the ISS) derived from the assumptions in table 1.4.

1.5 Requirements for the photo-detector

In this report the word *photo-detector* will be taken to include the following systems:

- the focal surface layout and engineering, its integration with the support structure and with the space vehicle;
- the optical interface on the focal surface (the light collection system);
- the sensors;
- the front-end electronics;
- the ancillary systems required for the proper functioning and control of the photo-detector and for data acquisition.

The choice of the best photo-detector for the observation from space of the EAS produced in the atmosphere by very high-energy cosmic rays [1] is a very difficult challenge, due to the many requirements and constraints.

The photo-detector has to be able to detect EAS by observing the nitrogen fluorescence light produced during the EAS development and the Cherenkov light reflected from the Earth surface. It must be able to determine the position of the arriving photons as a function of time to be able to follow the space-time development of the EAS. The main requirements are summarized below.

- The photo-detector must have single photon sensitivity in the $330 \div 400$ nm wavelength range to detect as faint as possible EAS, because this affects the energy threshold. In this wavelength range the atmosphere is relatively transparent.
- The photo-detector must have a fast response (well below ≈ 0.1 μs) to follow the space-time development of the EAS and to be able to determine the EAS direction from one single observation point.
- Only a moderate spatial resolution (of the order of the mm) is required, due to the desired pixel size.
- The photo-detector must have a low noise and good signal to noise ratio to detect the faint signal produced by the less energetic EAS and to discriminate it from the background. Small cross-talk and after-pulse rate are required.
- A good and uniform detection efficiency is required.

- It must have a large area (of the order of a few square meters), due to the large field of view required to the optics, and it must cover the focal surface with a sensitive area as large as possible, reducing dead or inefficient areas. The curved focal surface can be more easily covered by a mosaic of small units.
- The large field of view and the desired spatial granularity require a large number of pixels (hundreds of thousands) and therefore a complex read-out electronics, capable to handle such a large number of channels, is required.
- Low power consumption is required.
- Low mass, mechanical robustness and small dimensions are required.
- Space radiation tolerance is required.
- It must have a low sensitivity to magnetic fields of the order of the gauss.
- It has to be highly reliable and stable over long periods (a few years).
- It has to be compatible with the requirements imposed by a space mission.

Chapter 2

Sensors for the *EUSO* photo-detector

A number of possible sensors exist for use in the EUSO photo-detector [7–9]. However, after a preliminary review, only a small number remained as possible candidates, taking into account the requirements of section 1.5. They are discussed below.

2.1 The Hamamatsu R5900/R7600 Multi-Anode PhotoMultipliers Tubes

Commercial Multi-Anode PhotoMultipliers Tubes (MAPMT) are available [6] from Hamamatsu K. K. with characteristics close to the above requirements, in particular concerning the pixel size, the gain, the fast response time and the low mass and dimensions of the device. The most recent devices also show a very low cross-talk and good uniformity in the response. Unfortunately the present devices have a low sensitive to total area ratio, typically less than 0.5. An $R\&D$ program is under way to find possible solutions to the problem (see section 3.2.1). The small number of channels of commercial devices (≤ 64 channels per devices) requires a close packing of a very large number of small devices on the focal surface. If the focal surface is curved the packing of the devices has to be optimised to reduce losses in the geometrical acceptance due to dead regions between the close packed devices. This makes the mechanical assembly difficult but it is required to fit a curved focal surface. A more detailed description of this devices will be given in section 3.

The devices have been extensively tested, recently, by many groups. Among the others they have been used in the readout of a cluster of 9 MAPMT to detect Cherenkov light in a test-beam setup by the RICH-LHCb Collaboration at CERN [10], in the framework of a RICH detector development and design.

2.2 Hybrid Photon Detectors (HPDs)

Hybrid Photon Detectors (HPDs) have also been considered as possible candidates fulfilling most of the requirements. HPDs use a silicon pixel detector to detect the photoelectrons emitted by a photocathode [11] after a suitable electrostatic acceleration and focusing.

Multi channel HPDs are now becoming reliable instruments. The LHCb/RICH group at CERN has been developing them, since many years, in collaboration with industry (in particular, DEP) [12,13].

In an HPD the photocathode is deposited on a spherical entrance window inside a high vacuum tube (residual pressure $\approx 10^{-7}$ Pa). Photoelectrons are accelerated and focused by an electrostatic field (about 20 kV), compressing the photocathode image and providing the photoelectron with the required energy. Photoelectrons are collected on a silicon pixel detector bump-bonded or wire-bonded to a readout chip, both placed inside the vacuum tube.

HPDs features a linear and stable gain coming from a dissipative process, with a threshold of the order of the kV. For an applied voltage of ≈ 20 kV the gain is $\approx 5 \cdot 10^3$. They show a very good single and multiple photoelectron response, with well separated peaks, allowing precise photon counting. The power consumption is very low as the device draws virtually no current but a very high voltage is required which affects the device gain. The response is uniform in position with less than $\approx 10\%$ variation reported, and very fast ($\mathcal{O}($ ns$)$). The device allows a flexible pixel layout design.

HPDs are being developed for various applications, from scintillating fibers readout to biomedical applications.

Recent reports of their development can be found in [12,13].

There are however a number of critical items with HPDs which require further investigation and R&D. HPDs, compared to MAPMT, require a higher voltage to be operated and provide a smaller signal with the consequent need of a more sophisticated read-out electronics and very low-noise charge amplifiers. The mechanical robustness under vibration and/or shock, including the reliability of bump/wire bonding, has to be checked. The removal of the heat produced by the electronics chip located inside the tube has, most probably, to be achieved by means of thermoelectric (Peltier) cooling. The high vacuum required and the overall operational and long-term stability are additional items which should be investigated for operation in space.

The use of HPDs in *EUSO* would certainly require some $R\&D$ and time and therefore they probably cannot be considered a viable solution for *EUSO* in the very short time.

2.3 Flat Panels PMTs

Flat Panel PMTs [14] represent a very appealing solution but as of today they are not yet released on the market [15]. Anyway their use in an AirWatch-type detector will require a careful investigation of some points, in particular their space qualification.

2.4 Conclusion

We have proposed to use commercial MAPMT for the *EUSO* photo-detector [16]. As of today commercial MAPMT are the most viable option for the photon detector. MAPMT are a well established technology, available from shelf, with a solid basis in industry and characteristics and a price which are easily quantified. They fulfill the requirements of high speed, low noise, low mass and small dimensions. Devices are now available with the required pixel dimension, low cross talk and good channel to channel uniformity. Their high gain allows to use a simple front-end electronics.

Therefore they seem to provide a viable solution.

Other alternatives are appealing but they are not ready for use is the short period.

Chapter 3

Features of the MAPMT and use in *EUSO*

3.1 The Hamamatsu R5900/R7600 MAPMT in *EUSO*

Hamamatsu Corporation produces MAPMT (R7600 [17]) with different pixel sizes. The physical dimension of the MAPMT section is 25.7×25.7 mm^2 and the length is about 33 mm. The tube is equipped with a bialkali photocathode and a UV-transmitting window 0.8 mm thick. This would ensure good quantum efficiency for wavelengths well below 300 nm, with a peak of about 20% at a wavelength of 420 nm. The device has a Metal Channel dynode structure with 12 stages, providing a gain of the order of 10^6 for a 0.9 kV applied voltage using a standard tapered voltage divider. This large gain allows to use a simple front-end electronics, without the need for sophisticated fast, low noise and low power preamplifiers. According to the data sheets the anode pulse rise-time is ≈ 1 ns and the transit time spread ≈ 0.3 ns. Cross-talk is $\approx 2\%$ and pulse amplitude non uniformity between different anodes is $1 : 2$. The mass is $\simeq 30$ g. The overall anode dark current after 30 minutes storage in darkness is of the order 20 nA. The availability of different pixel sizes proves to be extremely useful to match the PSF of the optics.

The device with the largest number of pixels (R7600-M64) has 8×8 square pixels of 2 mm side and 2.3 mm pitch, giving a 18.1×18.1 mm^2 maximum sensitive area. Between any two rows of pixels there is a low efficiency region about 300 μm large.

Devices with a larger (that is twice and four times) pixel size are available. The R7600-M16 has 4×4 square pixels of 4 mm side and 4.5 mm pitch, giving a 17.5×17.5 mm^2 maximum sensitive area. Between any two rows of pixels there is a low efficiency region about 500 μm large.

In both cases the ratio between the sensitive area and the total area (geometrical acceptance) is ≈ 0.45, assuming an average efficiency in the inter-pixel regions equal to one

half the maximum efficiency.

The R5900/R7600 data-sheets are shown in the appendix in figures 7.1, 7.2, 7.3, 7.4.

3.2 Open items and possible solutions

3.2.1 Geometrical acceptance

A preliminary $R\&D$ program has been carried on to find possible solutions to the problem of the low overall geometrical acceptance of the MAPMT (see the section 3), which would strongly limit the usefulness of the bare commercial device and appears to be the main limiting factor to the use of the device in our application.

Actually the main problem is not the low overall geometrical acceptance but the fact that the geometrical acceptance would be highly non-uniform on the focal surface by using only the bare devices. In fact the focal surface would consist of sensitive regions, at the center of each MAPMT, separated by the totally blind regions on the edge of the device. As one pixel will cover about $0.5 \div 1$ km at the Earth surface and the length of a typical EAS is up to a few tens of km, a large fraction of the EAS would not be fully detected, seriously compromising the observational capabilities.

The geometrical acceptance could be improved by means of a suitable light collector system, to be placed in front of each device, and performing the required demagnification onto the MAPMT sensitive area. This system might consist of a lens system, a system made of a bundle of tapered light pipes (working either by normal reflection or by total internal reflection) or a fiber optic taper.

As a design objective an overall geometrical acceptance of the combined light collector system plus MAPMT of $\simeq 0.5$ will be assumed, but requiring a good uniformity on the focal surface.

In what follows the use of the M64 MAPMT is assumed, as it provides the maximum pixel density. The use of the M16 version would make the design of the lens even easier due to the bigger pixel size (allowing to accept larger distortions) and to the smaller number of channels (requiring a less complex device in case a bundle of tapered light pipes is used).

3.2.1.1 Tapered light pipes system

The Winston cone [18] has been used since a long time to collect light on photomultiplier tubes. As the Winston cone is a non-imaging system it cannot be used on the MAPMT as a whole. One single tapered light pipe per pixel has to be used, in a multiple Winston cone arrangement. This might exploit either the total internal reflection inside a refractive and transparent light guide or normal reflection on the walls of an empty pipe

(either metallic or based on multi-layers dielectric coatings).

The use of this kind of light collector would have the advantage to remove dead regions on the focal surface, providing a more uniform efficiency, and to avoid the low efficiency regions between pixels. In addition to that it might help to fit a curved focal surface, by suitably shaping the entrance window of the pipes.

The maximum achievable demagnification depends on the angular spread of the incoming rays and on the refractive indexes of the involved materials. Squeezing the cross section of a bundle of photons gives rise to a corresponding increase in the angular divergence of the bundle, setting a limit to the total allowed demagnification [18].

One possibility is then to assemble a system made of 8×8 square-section tapered slanted light pipes, one for each pixel, in such a way that each pipe has an exit face with the same dimensions of the MAPMT pixel, and and entrance face with dimensions of $1/8 \times 1/8$ the 25.7×25.7 mm^2 corresponding to the physical dimensions of the MAPMT. Actually the dimension of the exit face can be slightly smaller than the pixel dimension, to concentrate the photons on the central, more efficient region of the pixel. Similarly the entrance face might be slightly larger to recover the unavoidable clearance in the MAPMT packing and to optimise the packing of the devices on a curved focal surface.

The bundle of light pipes should be arranged in such way that a one to one mapping between 8×8 ideal square pixels on the focal surface and the real 8×8 square pixels of the MAPMT is obtained. Each pipe would have the shape of a truncated skew pyramid with square bases. Such an arrangement would leave some distance among the neighbouring pipes, useful to avoid the 300 $\mu\mathrm{m}$ low efficiency region between the MAPMT pixels. This space should be kept at a minimum on the entrance side, to reduce the geometrical inefficiency, and may increase to about 300 $\mu\mathrm{m}$ or slightly more at the exit side. In what follows the meaning of *length of the pipes* is the distance between the two parallel planes defining the entrance and exit faces of the pipe, that is the two basis of the pyramid, and not the length measured along the axis (which would depend on the geometry of the specific pipe).

The system based on tapered light guides has the advantage that the imaging from the focal surface to the photocathode is not distorted inside the pixel granularity. Moreover the inefficient region between pixel and pixel is recovered. Finally no additional surface is added (and reflection losses are therefore not worse than with the MAPMT alone) in the case of the system based on normal reflection and in the system based on total internal reflection, provided one can make an optical coupling to the MAPMT input window.

3.2.1.1.1 Total Internal Reflection tapered light pipes system. The first possible implementation is by means of solid transparent pipes working by total internal reflection. As

the photons are driven to the MAPMT entrance window by total internal reflection a negligible loss is introduced at each reflection, provided the surface finish is good enough and the photon incidence angles are not violating the total internal reflection limit.

The entrance face of the pipes has to coincide with the focal surface of the main optics. It can be coated with an anti-reflection coating to decrease the reflection losses.

To minimize reflection losses and avoid total internal reflection on the exit face of the light pipe this should be in optical contact with the MAPMT input window. Optical coupling with the MAPMT input window is a critical point with this device. If this cannot be obtained light losses due to total internal reflection at the exit face of the pipe might occur, while the reflection losses might always be reduced by an anti-reflection coating.

If the length of the system is too short the rays might reach a point where the total internal reflection condition is violated and the rays will then leak out of the light pipe. On the other hand if the length of the guide is too long the absorption inside the pipe might become unacceptable, as well as its mass and dimensions. The length of the system is therefore one of the parameters which need to be optimised.

Optimisation of the system is under way. The performance of the external light pipes, the most critical as they have to produce the largest change in direction of the bundle of photons, could be improved by giving a suitable tilt to the entrance face.

Construction of the device. Possible methods to build the system are under study. The main requirement is not the mechanical precision, because the system is inherently stable for small variations from design values as long as one stays away from the critical conditions when rays start to be lost on the lateral walls because the total internal reflection condition is violated. The main requirements will be on the smoothness of the walls, to reduce imperfections which would cause ray losses, and on the good optical coupling with the MAPMT entrance window.

One possibility is to assemble the 64 pipes by cementing on the entrance and on the exit face of the pipes a thin sheet of the same material the pipes are composed of. The sheet on the entrance face would slightly degrade the performance of the system, by making the space resolution slightly worse, because the first refraction would take place slightly before the light pipe starts. The sheet on the exit face would produce some light loss because photons exiting from the pipe might miss the MAPMT sensitive region due to the fact that the photocathode would be at some distance from the exit face of the pipe.

This kind of device could be made also in quartz (see section 3.2.1.4), but in this case it might turn out to be quite expensive [20]. A cheaper possibility is provided by the use of the Sol-Gel technology (see section 3.2.1.4). In both cases mass might be an issue.

3.2.1.1.2 Reflecting tapered light pipes system. The same geometry discussed for the total internal reflection tapered light pipes system might be used for a system exploiting normal reflection on the walls of a bundle of empty pipes. This kind of system would have the advantage of no absorption and no limits due to total internal reflection requirement. However the number of reflection requested, the fact that the reflection coefficient is normally dependent on the incidence angle, the large range of the angles of incidence of the photons on the reflecting walls and the requirement of a very good reflectivity require a very good coating to avoid unacceptable light losses preventing the use of such a system.

Construction of the device. A simple prototype for the 4×4 version was recently built by assembling thin aluminium sheets [21]. In the real device one has to include the inefficiency produced by the thin sheets making the walls which does not exist in the total internal reflection tapered light pipes system. Extrapolating the parameters of the prototype to the 8×8 version one immediately gets a loss of 28%, which might be possibly improved by using thinner sheets. However due to the required mechanical properties it is difficult to imagine that this figure can improve too much.

Another possibility might be to build the device by moulding, followed by an appropriate coating of the internal faces.

3.2.1.2 Lenses

Another option to recover the geometrical acceptance of the MAPMT is by using lenses in front of it.

One possible system consists of a plano-convex hemi-spherical lens located in front of the MAPMT with the curved face of the lens facing the incident rays and the plane face in optical contact with the MAPMT input window and coincident with the original focal surface. Alternatively a small gap between the plane face of the lens and the entrance window of the MAPMT might be left, in case the optical coupling between the lens and the MAPMT turns out to be difficult to realize from the engineering point of view. A similar system was recently designed by the RICH-LHCb Collaboration at CERN [27,23].

In the paraxial approximation a hemi-spherical lens with the plane face placed on the focal plane of some objective will re-focus the incident rays on the same focal plane but with the image demagnified by a factor given by the refractive index of the lens material. A system of this kind is sometimes known in the literature as an *immersion lens* [19]. Assuming a refractive index $n = 1.5$ the required $\simeq 0.67$ demagnification is obtained. The radius of curvature of the lens is a free parameter to be optimised as a compromise between the need to limit aberrations (significant for a small curvature radius) and the need

to reduce absorption losses inside the lens (significant for large curvature radius).

For the present device a baseline radius of the lens of $20\ \mathrm{mm}$ is assumed. The lens will be a square with a slightly larger dimension than the MAPMT, to leave a little space between MAPMT required for the mechanical structure and a possible magnetic and/or electrostatic screen. This gives a maximum thickness of the lens of $20\ \mathrm{mm}$ on the optical axis. The minimum lens thickness, at the four corners, is given by the relation $t_{min} = \sqrt{R^2 - l^2/2}$ as a function of the lens radius, R, and lens side l. For the radius $R = 20\ \mathrm{mm}$ one has $t_{min} = 5.96\ \mathrm{mm}$, and the minimum possible lens radius is given by $R = \sqrt{l^2/2} = 19.1\ \mathrm{mm}$.

A view of the lens with some ray tracing, demonstrating the demagnification capabilities of the lens for different field angles, is shown in figure 3.1.

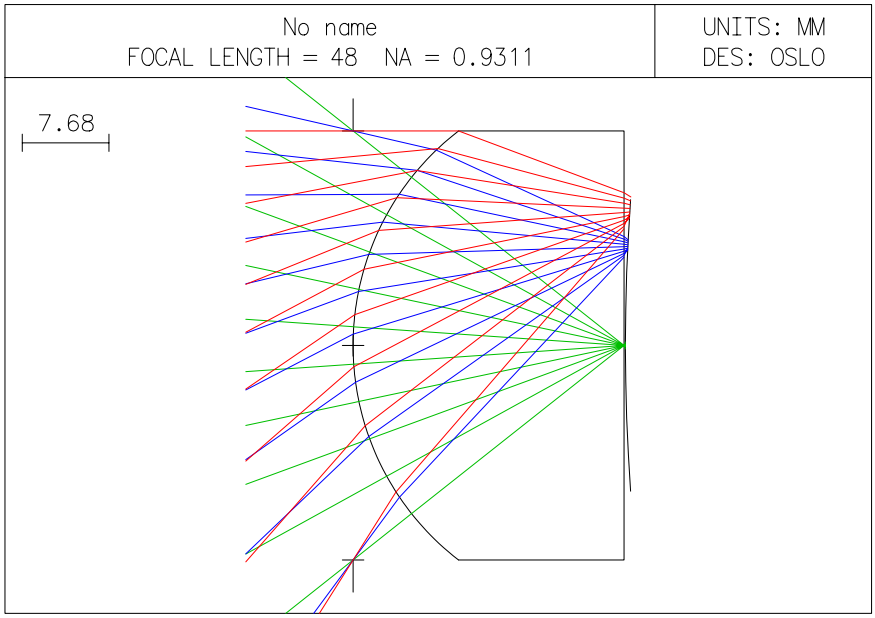

Figure 3.1: Ray tracing through the hemi-spherical lens (simulated with Oslo 6.04 from Sinclair Optics, Inc.). The ray-tracing clearly shows the demagnification capability of the lens.

Aberrations, geometrical as well as chromatic, are important but not critical, because of the low spatial resolution required (of the order of a few millimeters). The results of ray-tracing of a hemi-spherical lens are shown in figure 3.2.

The system is very attractive because it is very simple and cheap. It has however some limits whose effects have to be carefully examined. The inherent distortion of the

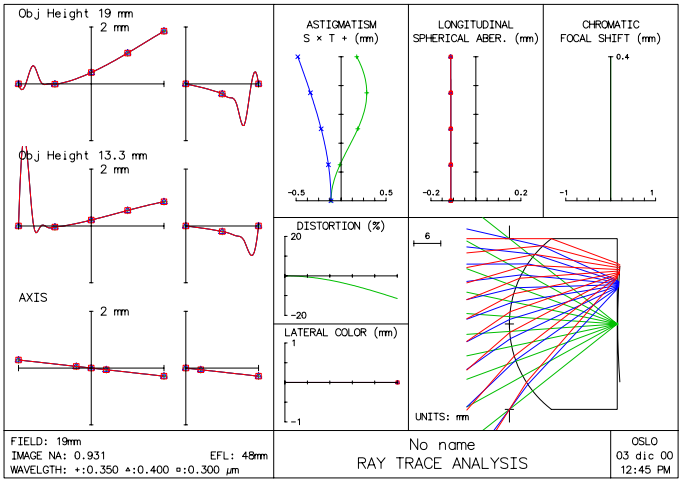

(a) Hemi-spherical lens: ray-tracing analysis

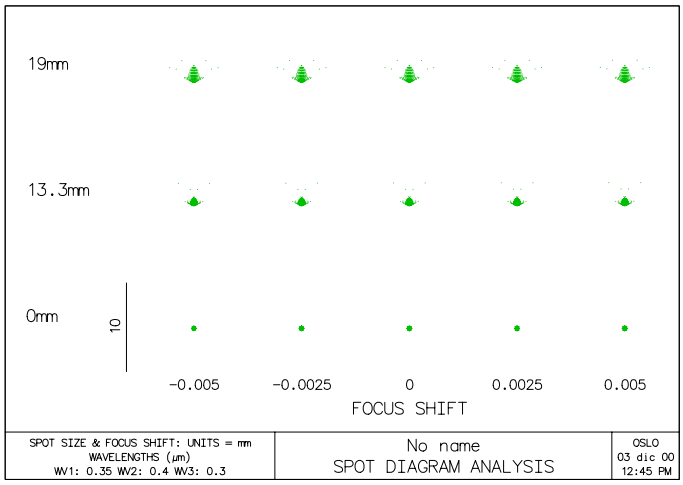

(b) Hemi-spherical lens: spot diagram analysis

Figure 3.2: Performance of the hemi-spherical lens (simulated with Oslo 6.04 from Sinclair Optics, Inc.): the first plot (a) shows the aberration curves and the second plot (b) shows the Point Spread Function.

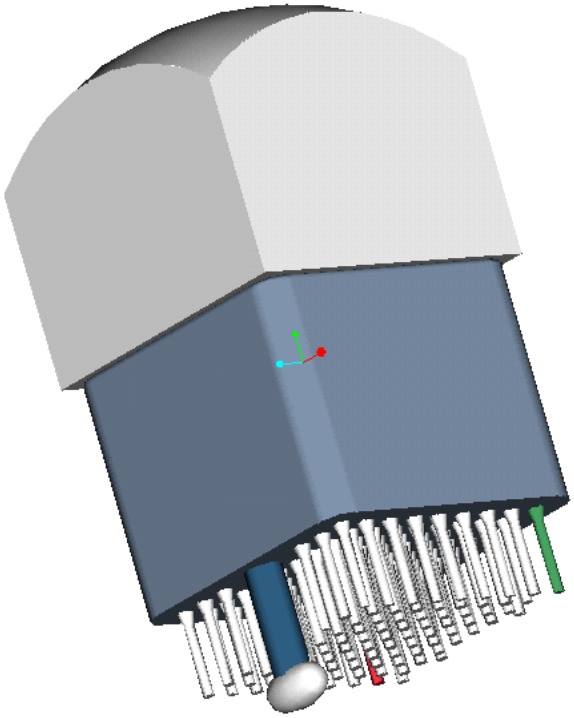

Figure 3.3: The hemi-spherical lens mounted onto the MAPMT.

image due to aberrations, however small, will make the space resolution worse. A fraction of photons will be reflected at the lens surface, instead of being refracted, with the additional possibility to be collected by another lens and increase the noise. The fact that a photon can reach the lens surface at any angle with the normal, might limit the usefulness of an anti-reflection coating, which should be a broad-band and broad-angle one. The spatial resolution might become worse if chromatic aberration would not be negligible.

A major problem is given by the shadowing effect of one lens to its neighbouring lenses for rays which fall close to the border between two lenses. In this case one ray might intercept the wrong lens, that is the ray might intercept not the lens lying on the MAPMT covering the focal surface region toward which the photon would be directed in case the lens is not present, but it might intercept one of nearby lenses. Therefore the photon would be focused and reconstructed onto the wrong region of the focal surface, introducing a degradation of the spatial resolution.

A view of the lens on the MAPMT is shown in figure 3.3 and a view of an array of MAPMT plus lenses is shown in figure 3.4.

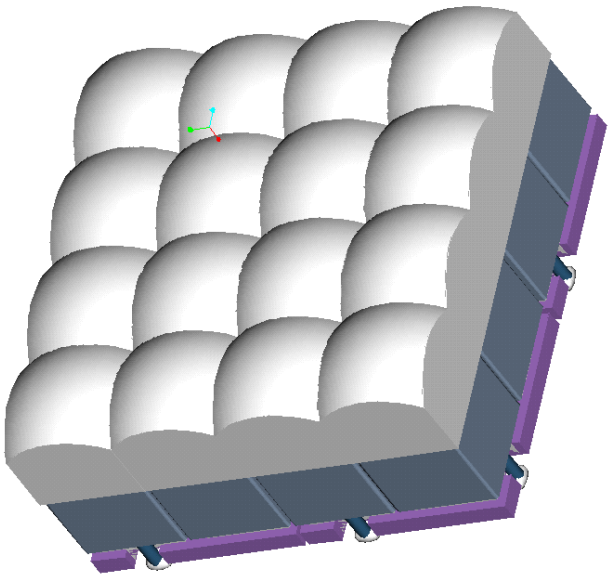

Figure 3.4: The array of MAPMT plus hemi-spherical lenses.

3.2.1.2.1 Prototypes and tests Prototypes have been built either using the Sol-Gel technology (see section 3.2.1.4) and as classic quartz lenses.

The Sol-Gel lenses are under test to ensure they satisfy the requirements, in particular concerning the bulk transmission, mechanical precision and surface finish.

The classic quartz lenses have been used in the readout of a cluster of 9 MAPMT to detect Cherenkov light in a test-beam setup by the RICH-LHCb Collaboration at CERN [10].

3.2.1.3 Fiber optics tapers

Fiber optic tapers might be used to demagnify the image from the focal surface onto the MAPMT sensitive area. The main limits of commercial fiber optic tapers are that they are normally made for use in the visible and that the filling factor of the entrance face (sensitive to total area ratio) is normally of the order of 0.75 [22]. An R&D would be required to investigate the possibility to build fiber optics tapers with a material having the required transmission in the near-UV.

3.2.1.4 Choice of the materials and engineering issues

The optical coupling between the system and the MAPMT input window is not trivial due to the rather large deviation from planarity of the MAPMT input window.

As the Hamamatsu technical specifications do not provide details about the flatness of the MAPMT input window, nor about the parallelism between the input window and any reference surface on the MAPMT itself, some measurements were made on some MAPMT [23]. The measurements were performed on two MAPMT with borosilicate window and one MAPMT with UV-extended borosilicate window. After scanning the MAPMT window with a step of about $2\ \mathrm{mm}$ in two directions roughly parallel to the MAPMT sides the data were fitted to a plane. The maximum distance, in the direction perpendicular to the fitted plane, between any two points was found to be 0.02 mm, for the MAPMT with UV-extended borosilicate window, and 0.03 mm for the two MAPMT with borosilicate window.

The performance of any light collection system is strongly dependent on the availability of material with the right optical properties. In fact a successful reconstruction of the events requires that the light losses are kept to the minimum. Bulk absorption inside the light collection system can be easily estimated, after the material has been chosen.

3.2.1.4.1 Reflecting tapered light pipes system. An UV-enhanced aluminium coating would provide a reflectivity of about 0.9 at normal incidence in the near UV. Assuming, very roughly, this figure as an estimate for the average reflection coefficient one can see that five reflection already provide an overall attenuation of about 0.4.

A coating based on dielectric layers would be required but the large range of the angles of incidence of the photons would require a very high reflectivity in a large range of angles, up to grazing incidence in the full band of interest.

3.2.1.4.2 Lens and Total Internal Reflection tapered light pipes system. The two systems share the same requirements concerning the choice of the materials. This is the same problem of the main optics, where highly transmitting materials in the $330 \div 400\ \mathrm{nm}$ wavelength range are required, either for the Fresnel lenses and for the corrective plate of a Schmidt camera.

Quartz would not give any problem for the transmission but would significantly increase the mass. The Sol-Gel silica technology [25,26], allowing to produce high purity silica optics by means of a moulding process, might be used. In both cases mass might be a problem.

Polymers have become recently available having good physical qualities, see [4].

3.2.1.5 Simulations.

Preliminary simulations of the performance of the different light collection systems have been carried on, in order to have a first evaluation and comparison of their performance.

The simulation was carried on having in mind the 64 channel version of the MAPMT. A plane bi-dimensional array of MAPMT was used, with a pitch of 27.0 mm between MAPMT, larger than the real MAPMT side to leave room for the needs of the engineering of the photo-detector surface. The average relative efficiency in the inter-pixel regions of the MAPMT is assumed equal to one half the maximum efficiency.

A bunch of photons was simulated, falling onto the MAPMT bi-dimensional array at an average incidence angle of zero to the normal, uniformly distributed in solid angle and with different maximum incidence angles ($20°, 25° and 30°$). The photons are unpolarized and their wavelength is assumed to be 350 nm in the present simulations.

An array of MAPMT without any light collection system, with a 27 mm pitch, would provide an overall photon detection efficiency of about 39%, taking into account the dead region around the photo-cathode and assuming an average efficiency in the inter-pixel regions equal to one half the maximum efficiency and reflection losses of 3% at the MAPMT input window.

3.2.1.5.1 Results of the simulations: total internal reflection light pipes. The exit face of each pipe is assumed to be 0.1 mm shorter than the pixel size, to avoid the lower efficiency region at the edges of the pixel and to reduce the light losses. In fact some photons miss the sensitive MAPMT area because the photocathode is necessarily located at some distance from the pipe exit face. The 0.5 mm plate on the exit side is separated, conservatively, by a 1 mm empty gap from the MAPMT input window, the effect of the latter being fully simulated. This is a rather conservative figure indeed, which has the effect that many photons are lost because they fall into the low efficiency inter-pixel region.

Note that to a first approximation the results also apply to the M16 version of the MAPMT, as in that case all transverse dimensions scale by about a factor two, compared to the present one, and the performance of the light collector is mainly determined by the ratio of the input and exit areas as well as by the incident angle distribution. Rigorously speaking it also depends slightly on the ratio between the transverse and longitudinal dimensions of the pipe, which in the present case does not scale.

It is assumed that two thin plates, 0.5 mm thick, are placed both at the input face and at the exit face of the collector to mechanically assemble the pipes, without introducing any light attenuation at the interface between the pipes and the plates [20].

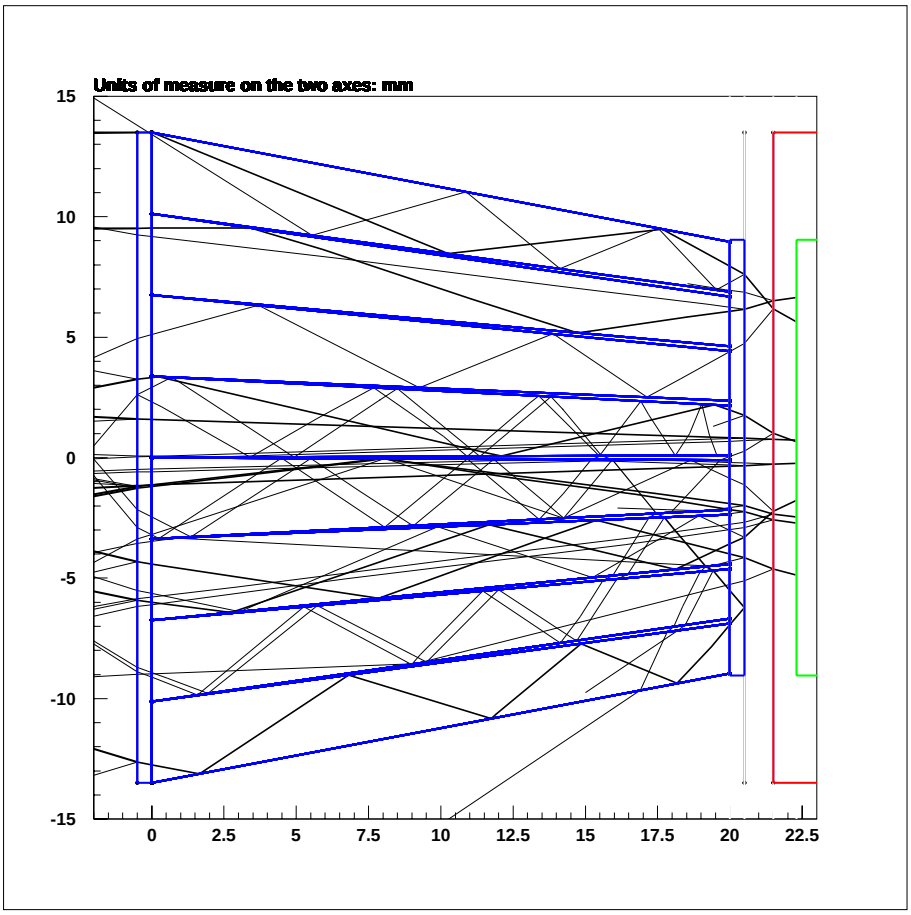

Figure 3.5: Ray tracing in the total internal reflection light collecting pipes. The length of the pipes is 20 cm. A ray is followed, with all its branchings, until its relative intensity goes below 3%. The *blue* drawing indicates, schematically, the light pipes assembly, the *red* contour simulates the MAPMT physical dimensions while the *green* area indicates the photocathode. The line thickness approximately simulates the relative ray intensity. Units are mm.

The tracing of a few rays, for illustrative purposes, is shown in figure 3.5.

Note that in the figure the space between the pipes is assumed to be completely transparent but this is not the case in the simulations. The simulations assume that photons violating the total internal reflection condition somewhere inside the pipe are absorbed before reaching any other pipe. If this is not the case they will produce cross talk in the neighbouring pipes.

The light collection efficiency for different length of the pipes and for bundles with different maximum incidence angle is shown in table 3.1. Note that total internal reflection on the exit face, particularly significant for short pipes, might be reduced by optically coupling the light collector system to the MAPMT input window. In addition the reflection

losses at the entrance and exit faces can be reduced by a suitable anti-reflection coating.

$\theta_{\max}$	$l = 10$ mm	$l = 20$ mm	$l = 30$ mm	$l = 40$ mm	$l = 50$ mm
20°	0.45 (0.78)	0.66 (0.85)	0.72 (0.87)	0.72 (0.88)	0.75 (0.89)
25°	0.41 (0.77)	0.60 (0.83)	0.66 (0.86)	0.72 (0.88)	0.71 (0.88)
30°	0.42 (0.77)	0.60 (0.82)	0.68 (0.84)	0.70 (0.86)	0.68 (0.86)

Table 3.1: Light collection efficiency for different length of the pipes and for bundles with different maximum incidence angle. The reflection losses at the three refracting surfaces and from partial (instead of total internal) reflection inside the pipes as well as total internal reflection on the exit face are all included and their contribution is the number in parentheses. The statistical errors from the finite sample size is, in all the cases, 0.02.

The bulk absorption inside the pipe material is not included. Anyway it can be easily estimated, once the material has been chosen, by just taking into account the pipe geometry.

The results show that an overall efficiency up to $\approx 70\%$ can be reached for the bunch of photons with 20° maximum incidence angle with a 30 mm long pipe, close to the one expected from the EUSO optics. This takes into account all the losses (assuming conservatively no anti-reflection coating on the entrance and exit faces), but those coming from the bulk absorption, which depends on the material.

3.2.1.5.2 Results of the simulations: reflecting light pipes. A reflecting light pipe system has been simulated as well. A constant reflectivity on the walls, equal to 0.9, was assumed, independent of the incidence angle and wavelength. This is quite a rough assumptions but the assumed average reflectivity is probably close to the maximum realistic values. The final light collected is attenuated by the reflection losses.

The MAPMT input window was properly simulated and the exit side of the light collector system is supposed to be in contact with the MAPMT input window (just a mechanical contact is required).

Table 3.2 summarizes, for different length of the pipes and for bundles with different maximum incidence angle, the performance of the system. The results are split between the purely geometrical efficiency, which only depends on the distribution of the incidence angle of the photons and the geometry of the collector (the first number), and the attenuation due the reflection losses on the walls (the second number). The second factor, in fact, is strongly dependent on the wall reflectivity as a function of wavelength and incidence angle. However the assumed 0.9 is probably close to the better achievable reflectivity. The reflection losses at the MAPMT entrance window are included in the second number as well as the effect of the inefficient MAPMT inter-pixel regions.

An additional loss has to be included, due to the finite thickness of the reflecting walls, which implies some loss in the geometrical acceptance at the entrance face, as discussed in 3.2.1.1.2.

$\theta_{\max}$	$l = 5$ mm	$l = 10$ mm	$l = 20$ mm	$l = 30$ mm	$l = 40$ mm
$20°$	$0.54/0.69$	$0.82/0.68$	$0.87/0.65$	$0.90/0.58$	$0.88/0.51$
$25°$	$0.51/0.70$	$0.77/0.67$	$0.87/0.59$	$0.88/0.50$	$0.87/0.43$
$30°$	$0.55/0.70$	$0.75/0.67$	$0.84/0.54$	$0.91/0.44$	$0.90/0.36$

Table 3.2: Simulation, for different length of the pipes and for bundles with different maximum incidence angle, of the overall geometrical collection efficiency (first number) and attenuation due to reflection losses on the walls, assuming an average reflectivity of 0.9, and reflection losses at the MAPMT entrance window (the second number). The statistical error from the finite sample amount to 0.02 for all the numbers in the table.

The results show that the overall efficiency up to $\approx 55\%$ can be reached for the bunch of photons with $20°$ maximum incidence angle, close to the one expected from the EUSO optics with the assumed average reflection efficiency.

3.2.1.5.3 Results of the simulations: hemi-spherical lens. An array of lenses with square section, side $l = 26.7$ mm, a pitch between MAPMT/lenses of $\Delta = 27.0$ mm and a 0.3 mm total absorption layer between the lenses was simulated, with different radii of curvature (20mm , 22mm , 24mm and 26mm).

The lens material is assumed to be a highly transmissive one, and bulk absorption is estimated as a stand-alone overall loss because this depends on the chosen material and it only contributes as an overall multiplicative factor. An empty gap of 1 mm was assumed, conservatively, between the lens and the MAPMT input window, to be conservative in case an optical coupling between the lens and the MAPMT input window is not feasible. The 0.8 mm MAPMT input window was simulated as well.

The results of the simulation are shown in table 3.3. These results apply to the M64 version of the MAPMT. In the case of the M16 the distortions are much less relevant due to the large pixel size.

The reflection losses at the two lens faces and the MAPMT input window, are not included in the numbers quoted in table 3.3. However they have been fully simulated and they amount to 11%, for all the combinations listed in table 3.3. Part of these losses might be recovered by a suitable anti-reflection coating on the two lens faces. The reflection losses at the MAPMT input window are present independently from the lens. The relative intensity of the reconstructed rays for a lens radius of 24 mm is shown in figure 3.6, for the same maximum incidence angles in table 3.3.

θ_{max}	$r = 20$ mm	$r = 22$ mm	$r = 24$ mm	$r = 26$ mm
20°	0.868 ± 0.008 (0.69)	0.834 ± 0.008 (0.70)	0.802 ± 0.009 (0.71)	0.777 ± 0.009 (0.72)
25°	0.858 ± 0.008 (0.65)	0.819 ± 0.008 (0.66)	0.777 ± 0.009 (0.68)	0.744 ± 0.010 (0.69)
30°	0.807 ± 0.009 (0.58)	0.763 ± 0.009 (0.60)	0.715 ± 0.010 (0.62)	0.670 ± 0.011 (0.64)

Table 3.3: Geometrical collection efficiency and geometrical distortions of the lens system as a function of the lens radius and the maximum incidence angle. The reflection losses at the entrance of the lens, which amount to about 11% in all the cases, are not included. The number in parentheses represents the fraction of the reconstructed rays which are reconstructed in the right pixel, providing an indication of the distortions introduced by the lens. The rays which are not reconstructed in the right pixel are always reconstructed in one of the nearby pixels. The quoted errors are the statistical errors only from the finite sample size.

The same plastics used for the main optics are the best candidate material. The path length inside the lens, which determines the absorption losses, is shown in figure 3.7 for two different values of the lens radius and for a maximum incidence angle of 25°. The average path length inside the lens material is 17.5 mm, for a lens radius of 20 mm and 24.5 mm, for a lens radius of 26 mm.

The results must then be corrected for the inefficient inter-pixel regions. Assuming an average efficiency in the inter-pixel regions equal to one half the maximum efficiency the overall loss amount to 0.89. Note, however, that this inefficiency is not introduced by the lens itself.

The results show that an overall efficiency up to 69% can be reached after the lens inclusion, for the bunch of photons with 20° maximum incidence angle, close to the one expected from the EUSO optics. This takes into account all the reflection losses (which amount to 11%, and assuming conservatively no anti-reflection coating), the inefficient inter-pixel region but ignores the bulk absorption, which depends on the material.

The lens introduces a degradation of the spatial resolution corresponding to about one pixel (for the M64 MAPMT) for about one third of the reconstructed rays. The effect would be clearly smaller for the M16 type, due to the larger pixels. While the spatial resolution is about constant while changing radius and the maximum incidence angle, the overall acceptance degrades quickly increasing the lens radius and/or the maximum incidence angle.

3.2.1.6 Impact of the light collector on the photo-detector

In case the light collection system has to operate in an environment with a significant background from high-energy charged particles, the impact of the production of Cherenkov and scintillation light by fast particles passing through the collector has to be

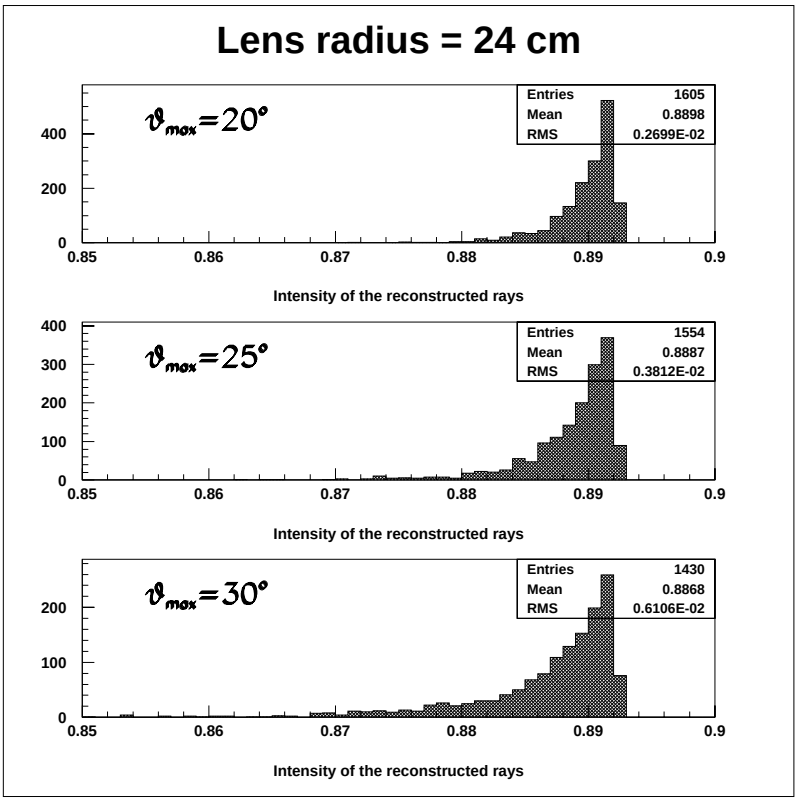

Figure 3.6: The relative intensity of the reconstructed rays. The lens radius is $24\ \mathrm{mm}$ and three different maximum incidence angle of the photons are considered.

studied. However in the case of *EUSO* a high-energy particle crossing the light collector system would produce a signal of very short duration (a few nano-seconds) compared to the much longer signal produced by EAS (of the order of micro-seconds).

The total internal reflection light pipe collector and the hemi-spherical lens collector, assuming they are made of quartz, have a mass roughly similar to the mass of the MAPMT alone while the mass is about halved if they are made of plastics. The reflecting light pipes system would have in any case a considerably lower mass.

3.2.2 HV polarity

Connecting the MAPMT in the anode grounding mode (that is with the anode grounded and the photocathode at a large negative potential) simplifies the readout circuit and improves its safety, by avoiding the use of HV decoupling capacitors. In this case the photocathode is at a large negative potential as the metal MAPMT case. This might require to keep at the same potential as the photocathode (and not to ground) any conductive struc-

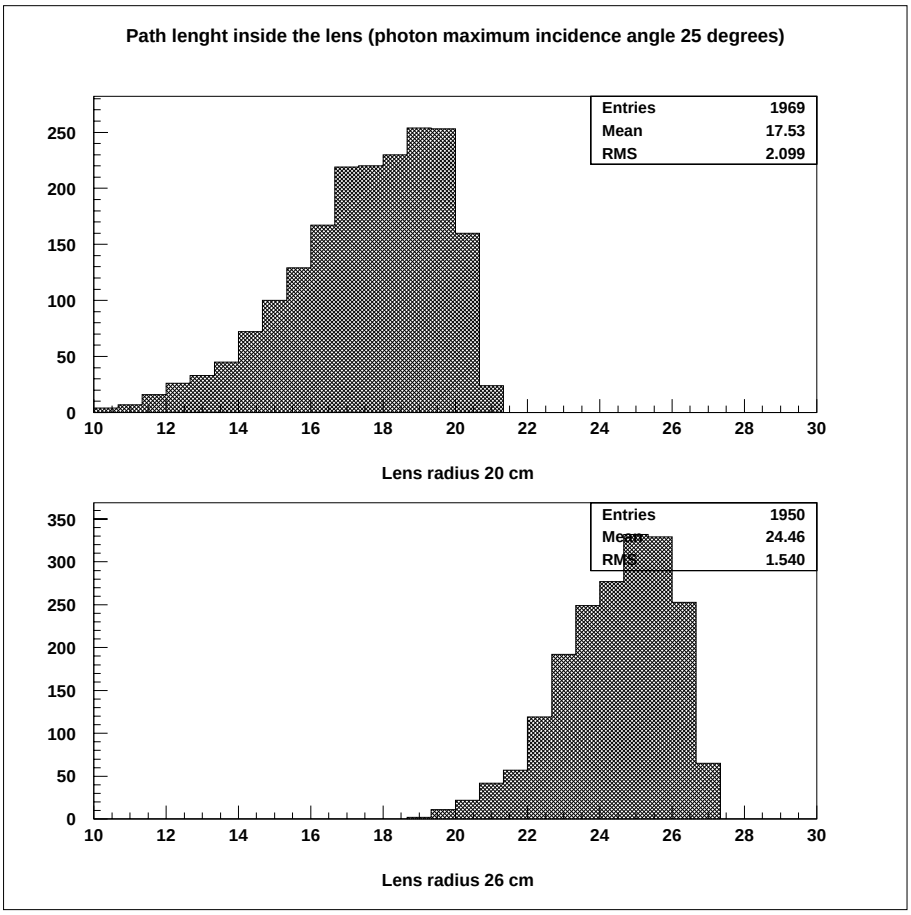

Figure 3.7: Path length inside the lens for two different values of the lens radius and a maximum incidence angle of the photons of 25°.

ture close to the MAPMT, such as any support structure as well as possible electrostatic and/or magnetic screens, which should extend beyond the MAPMT window by a length of about the MAPMT transverse dimension. If this is not the case the intrinsic MAPMT noise might increase. In addition to that the slight glass conductivity might cause current to flow between photocathode and ground, producing noise and possibly deteriorating the photocathode, in the long-term. With the MAPMT considered for *EUSO* these effects are mitigated by the presence of the metallic case, effectively acting as an electrostatic screen. Anyway the metallic case itself is at the same large potential as the photocathode. The MAPMT and the surrounding structure require in any case a careful insulation, also for safety reasons.

3.2.3 Gain variations (among pixels and among different MAPMT)

Two kinds of gain variations have to be considered. Average gain variations between different MAPMT and gain variations between different pixels on the same MAPMT. In both cases the maximum variation quoted by the manufacturer is about $2:1$, for the most recent devices.

Gain variations between different MAPMT can be treated with a standard solution. MAPMT with similar average gains are grouped together in a single module (for instance 2×2, see section 5.3.1). The average gain of the different modules are then equalized by tuning the HV of each module to obtain the desired gain. The fact that different modules will house MAPMT with different HV very close to each other might require to use electrostatic screens between different modules.

Gain variations among the pixels of the same MAPMT are accounted for by programmable discriminator thresholds (see section 4). The gain variations between pixels are dominated, normally, by a few outlying pixels, while the majority of the pixels show much more similar gains [15].

A calibration system has to be foreseen and it is under study.

3.2.4 Power consumption

The power consumption required to operate the MAPMT has to be determined by considering the average MAPMT anode current due to the average background light. Decoupling capacitors in parallel with the last dynode stages must then be sized to sustain the higher anode current needed during the short time when an EAS signal is detected. Note that with the present EUSO parameters, even when observing an EAS with $E \approx 10^{21}$ eV close to its maximum, one doesn't expect to observe, more than about one hundred signal photons, in a time interval of a few micro-seconds.

The bleeder current affects the PMT output linearity. The relative PMT gain variation is given, roughly, by

$$\frac{\Delta G}{G} \approx \frac{I_a}{I_b} \quad , \tag{3.1}$$

where I_b is the bleeder current and I_a is the anode current. In pulse operation decoupling capacitors, in parallel with the last bleeder resistors, help to maintain a linear output with a lower average bleeder current.

At low rates some output non-linearity is acceptable. It is acceptable in case of binary readout. In the case of *EUSO*, with binary readout and relatively low light levels, a high linearity of the output should not be required, except, possibly, for the analogue out-

put from one macro-cell [1], which is useful to improve the energy measurement of very high-energy EAS saturating the counting capability.

The total average anode current, that is the sum of the anode currents of all the MAPMT, can be estimated, in terms of the MAPMT gain, $G \approx 10^6$, the electron charge, e, and the other parameters in tables 1.4 and 1.4, and as a function of the total average background flux, B, as follows:

$$\overline{I}_a \simeq \frac{1}{2} D^2 \pi^2 \left[1 - \cos\gamma\right] B K_{opt} \varepsilon_{det} e G \quad . \tag{3.2}$$

Note that the atmospheric absorption, which might decrease the background flux on the photo-detector, has been conservatively omitted from the above formula, and the MAPMT gain has been conservatively assumed to be in the high range of the possible values.

With the standard parameters from tables 1.4 and 1.4, this gives a $6 \cdot 10^{10}$ Hz overall background rate (on the whole photo-detector) and $\overline{I}_a \approx 0.01$ A. Assuming to require $\Delta G/G = 0.1$, with an applied voltage of 0.9 kV the resulting power required is $P_{tot} \approx 10^2$ W.

The background rate on the single pixel depends on the number of pixels and, finally on the pixel size. According to the discussion in section 5 the number of channels may range from $1 \cdot 10^5$ to $4 \cdot 10^5$ providing a background rate on the single pixel in the range $0.15 \div 0.6$ MHz.

Even though this is a very small figure indeed, other considerations can help in case the above estimation is found to be too optimistic for any reason. The same applies in case one has to be more conservative than assumed above, for instance by requiring a larger $\Delta G/G$.

In fact the power consumption required to operate the MAPMT can be reduced by means of some standard methods. The standard Hamamatsu voltage divider ratio and anode grounding mode will be assumed in the following.

The power consumption can be decreased by reducing the current in the part of the bleeder circuit powering the first stages, where a high current is not required. Therefore two or more independent power supplies can be used to set the voltages of the resistor chain.

The simplest possibility (boosting of the last dynode stages) is to connect two power supplies with their positive terminals connected to the anode, the negative terminal of the first one to the photocathode and the negative terminal of the second one (the booster) to the dynode $\#12$, following the classical schemes in figure 3.8 (case (b)). The power consumption can be reduced by this method by about a factor three, compared to the case of

[1] A macro-cell is the name given to a logical assembly of a number of MAPMT as seen from the readout electronics [2,3].

one single power supply, by using the same voltage divider ratios. The resulting bleeder resistor chain has a total series value of $\approx 60\ \mathrm{M}\Omega$. A similar power consumption can be obtained by connecting to dynode $\#11$ or dynode $\#10$ but the required total bleeder resistance becomes larger.

In case the power is still too high and/or the output linearity is not good enough one can gain even more by using three (or even more) power supplies. The number of independent power supplies has to be optimised taking into account the low power requirements but also the complexity and reliability issue involved in using more power supplies.

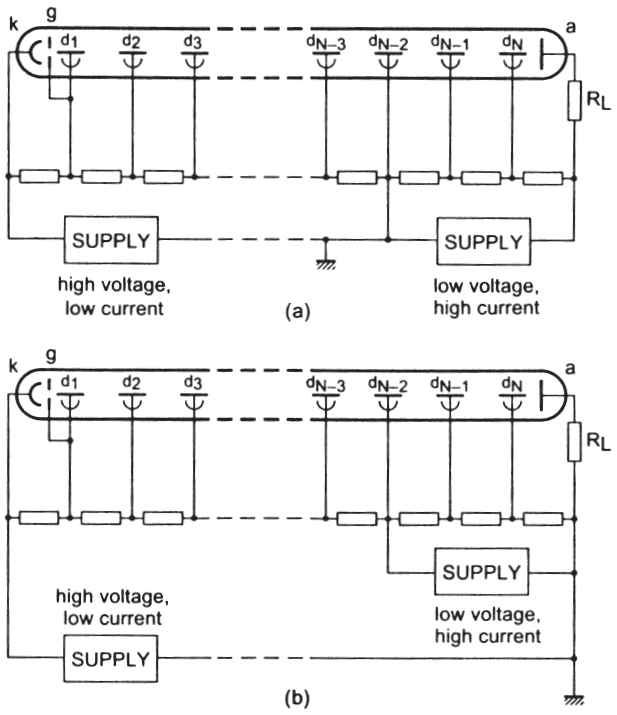

Figure 3.8: Voltage divider schemes for PMTs using two independent power supplies.

Others designs of the bleeder circuit exist, to improve the output linearity with lower power consumption, involving active dividers and Cockcroft-Walton generators.

Limiting the bleeder current also has the additional advantage to put an upper limit to the anode current, protecting the MAPMT from accidental over-currents from either unforeseen light or radiation flux on the MAPMT. In addition to that the power dissipated, which should be taken out in some way, is reduced.

The recovery time of the MAPMT after receiving intense light has to be carefully studied and its possible impact on the EAS detection capability evaluated.

A voltage divider optimised for *EUSO* has to be designed, built, and tested. The major required input to this is an estimation of the background light levels reaching the MAPMT as precise as possible. One needs a precise estimate of the total integrated incident light to tune the divider for minimum power consumption without compromising the signal detection, especially in case some kind of analogue readout channel (for instance one per MAPMT or one per macro-cell) is required for which the output linearity is more critical.

In this report it will be assumed, conservatively, that the MAPMT alone power demand is less than $200\ \mathrm{W}$, also taking into account the power supplies inefficiency.

3.2.5 Sensitivity to magnetic fields

The MAPMT output is sensitive to magnetic fields. The sensitivity to magnetic fields was measured by the LHCb/RICH group at CERN by measuring the MAPMT output inside an Helmoltz coil under different conditions [10]. The results show little sensitivity to transverse magnetic fields. Longitudinal magnetic fields of $\mathcal{O}(10)$ gauss give a sizable effect on the extreme rows of pixels. A magnetic field of $B \simeq 30$ gauss reduces their output to about 50%. The results are consistent with Hamamatsu measurements. A $0.9\ \mathrm{mm}$ μ-metal shield can recover the sensitivity when extending about $30\ \mathrm{mm}$ beyond the MAPMT window. A thinner screen would be enough for such a field intensity.

The average geo-magnetic field along the *EUSO* orbit is expected to be of the order of one gauss. However the effect of possible static and variable magnetic fields produced by the materials and devices, in *EUSO* and around it, has to be evaluated and taken into account in the engineering of the photo-detector.

3.2.6 After-pulsing

The incidence of after-pulsing has to be assessed. After-pulsing might in fact affect the photon counting and therefore the energy measurement.

3.3 Operational issues

3.3.1 Photo-Detector operation mode and optimisation

Due to the orbital period (about 1.5 hours) and to the stabilization time of the MAPMT after HV changes (about 30 minutes) the MAPMT have to be kept on at all times to avoid the operating instability connected with voltage changes.

The MAPMT should be operated at the lowest possible voltage to increase its lifetime, which depends on the total accumulated light. In fact the real levels of light which

the MAPMT will receive in orbit are not known with a great precision and therefore one has to be as conservative as possible. Operating the MAPMT at the lowest possible gain gives room to increase the voltage during the mission time to compensate for possible gain decrease due to ageing. Moreover operating the MAPMT at the lowest possible voltage also saves some power and reduces the intrinsic MAPMT noise. On the other hand the lowest gain is big enough for the front-end electronics (see 4).

Actually, by using the most recent front-end designs, one might even consider to operate the MAPMT at an even lower gain, saving lifetime and power. This might be accomplished by producing a MAPMT version with less than the standard 12 dynodes [15], thus reducing the gain. An even simpler solution might be to effectively reduce the gain, without modifying the MAPMT itself, by connecting together some of the central or last dynode stages through a resistor smaller than the one foreseen by the standard divider ratio. This effectively reduces the gain of the stage by changing its potential difference.

The signal from the last dynode might be used to take out the signal sum of all the pixels in one tube, useful for triggering purposes or to have a single analogue channel for MAPMT.

3.3.2 Ageing

The manufacturer provides data about the long-term operation stability of the MAPMT. The relative anode current change as a function of the operating time at an HV of $800\ \mathrm{V}$ and with an initial anode current of $100\ \mu\mathrm{A}$ (much larger the one expects in *EUSO*), shows a gain drop to 75% of the initial value after $\approx 10^4$ hours of operations. The ageing should be roughly proportional to the total collected charge. With an average background current $\lesssim 0.01\ \mathrm{mA}$ per MAPMT the expected tube lifetime should be compatible with the *EUSO* expected three years of operation especially if the tube can be operated at a lower gain to save power.

3.3.3 Space qualification

Results of test carried on at recently at CERN, Genova, Trieste and Palermo show a good agreement with the Hamamatsu specifications.

Photomultipliers of the same family (Hamamatsu R5900), with one single pixel, have recently been used in the AMS [28] detector, designed to be installed on the ISS, and whose test flight on the Space Shuttle has been recently carried on with success. The required mechanical robustness of the multi-pixel versions has to be verified, as the anode structure is one of the most delicate parts of the MAPMT.

3.4 Environmental aspects and MAPMT protection

Care has to be taken in order to protect the MAPMT from exposure to strong light, even when the devices are not operated and the HV are off, to avoid damage of the photocathodes and reducing the device lifetime. This is a non trivial issue, to be investigated with the mission specialists, due to the large field of view and large aperture of the optics.

Care has also to be taken to avoid strong thermal variations to avoid thermal stresses.

Radiation damage mainly implies glass browning. Data are available from the manufacturer [15]. UV-transmitting glass has better resistance than borosilicate glass. Therefore it is anyway recommended to use the UV-transmitting glass version.

Exposition of the MAPMT to significant Helium concentration has to be avoided because Helium diffuses through the glass. The possibility to avoid exposition of the photodetector to Helium at launch has to be studied, but no major problems are expected because PMTs have already been launched in space.

In case an open photo-detector structure will be used the effect of possible plasma (N_2, O_2 and electrons) and/or charged dust collection on the MAPMT insulating window and on the conductive parts has to be considered. If a closed photo-detector structure cannot be used a grid in front of the photo-detector surface set at an appropriate potential might be used to minimize the charge collection.

Chapter 4

The front-end electronics

4.1 Architecture of the front-end electronics

The front-end electronics is needed to preamplify the signals from the sensors, to discriminate these signals with a programmable threshold, to mask noisy channels, to provide information to the trigger system, possibly performing a first level trigger, and to store the information until readout is done.

The most important and critical features are the optimal gain and input impedance to match the photo-detector signal, the double hit resolution (required to be of the order of $10\ \mathrm{ns}$), the time information (with precision of the order of $10\ \mathrm{ns}$). Power consumption is a real challenge.

One should consider a highly integrated front-end chip for signal readout and possibly first level trigger. Required features are a very compact design with minimal distance between the MAPMT and the front-end electronics, a completely modular system with minimal cabling and self-triggering capabilities.

4.2 The *EUSO*/AirWatch front-end electronics

4.2.1 Introduction

EUSO is basically a large UV sensitive digital camera that must be able to take a high resolution picture at the MHz rate.

The very large number of active channels ($\approx 2.5 \cdot 10^5$ channels will be assumed for the present purposes, compare with section 5.4) and the requirements imposed by the space environment force to achieve a high level of modularity and integration of the front-end electronics.

In this section the work done in order to design and build a custom front-end chip for *EUSO* is described.

4.2.2 Requirements from Science

The basic idea of the *EUSO* experiment is to reconstruct the optical image of an EAS produced by an EHECR interaction in the atmosphere by looking at the nitrogen fluorescence light and the diffusely reflected Cherenkov light produced by the EAS by a suitable optical system installed on the ISS.

A suitable front-end and trigger electronics is required to read these signals and identify the EAS image above the continuous background [2,3]. The signal coming from an EAS must be disentangled above this continuum. Every EHECR develops an EAS that begins in the lower part of the atmosphere and arrive to ground moving effectively at the speed of light, that is $\approx 3\ \mu\mathrm{s}$ for every km.

The focal surface pixel linear dimension corresponds to about $0.5\ \mathrm{km} \div 1.0\ \mathrm{km}$ on the Earth surface (see section 5.4) giving a light track on the focal surface that persists on each pixel for a few $\mu\mathrm{s}$ up to a few tens of $\mu\mathrm{s}$, depending on the incidence angle and energy of the EHECR. In fact very vertical EHECR can be seen by a few pixels, so the persistence of the light in the same pixel can arrive up to a few tens of $\mu\mathrm{s}$. On the other hand very horizontal EHECR will move at the speed of light on the focal surface.

These figures fix the speed required to the digital camera. To get a good reconstruction power for the EAS one needs to take a picture roughly every $\mu\mathrm{s}$ (of course the true number still needs to be optimised).

Simulations show that the amount of light one can expect from very energetic EHECR ($E \approx 10^{21}\ \mathrm{eV}$) can be as high as a few hundreds detected photons in one $\mu\mathrm{s}$ at the shower maximum.

This means that one must be able to measure the amount of light collected by each pixel, either digitally, by counting the number of photons detected, or analogically, by integrating the charge and reading it out with a fast ADC.

The tight power limitations imposed by the space environment seem to rule out the second of these options, because it looks presently very difficult to have $2.5 \cdot 10^5$ fast ADCs running at $1\ \mathrm{MHz}$ with a total power budget below $300\ \mathrm{W}$. It was then decided to pursue the first option.

4.2.3 Basic design guide-lines for the *EUSO* Front-End Electronics

The large number of channels, the limited amount of space available, and the very strong power limitations strongly suggest to build a dedicated custom front-end chip. For compactness and modularity, it is highly desirable that this chip has the same number of channels of the MAPMT or a integer multiple of it. The design goals are the following.

- The chip should be DC coupled to the MAPMT. The MAPMT single photoelectron signals are expected to be $\approx$ 100 fC. The signal time width is about 5 ns, corresponding to $\approx$ 1 mV over 50 Ω or to a peak input current of $\approx$ 30 μA. The rise time is about 2 ns. The maximum signal input may arrive to a few hundreds of photons.

- Each channel, after a suitable preamplifier, must be able to discriminate the input signal with a programmable threshold.

- The gain of the input preamplifier of each channel is left undetermined and must be properly chosen at design time. What one needs is the ability to discriminate single photoelectron signals with threshold of about $1/3$ the single photoelectron signal.

- The discriminator should be fast enough to disentangle double hits as close as $10 \div 20$ ns. A double hit resolving time of $\simeq$ 10 ns would be perfect, while $\simeq$ 20 ns is close to the maximum acceptable for the physics requirements. A trade off is probably required to match this requirement and the next one which deals with the limited power consumption.

- The total power available under normal running conditions should be below $\approx$ 1 mW per channel. This requirement is strictly forced by the electrical power availability on the ISS (but similar considerations would apply to a free flying satellite).

- The final design should be radiation hard for three years of operation in space.

- The digital part of the chip is not specified in detail, yet. One will certainly need the ability to count the hits for each channel with a programmable threshold and to provide a fast-OR of the whole chip and of the individual columns and rows. The ability to store the data in some kind of memory or shift register would be desirable but this will be restricted by power limitations and by space availability on the chip. Possible design choices are described in the following sections.

- Each chip should be able to accommodate at least 64 channels (if the M64 version of the MAPMT is used). A channel modularity of 128 or 256 would be welcome.

4.2.4 Minimal configuration

Figure 4.1 shows a very schematic block diagram of this chip in a *minimal* configuration [2,3].

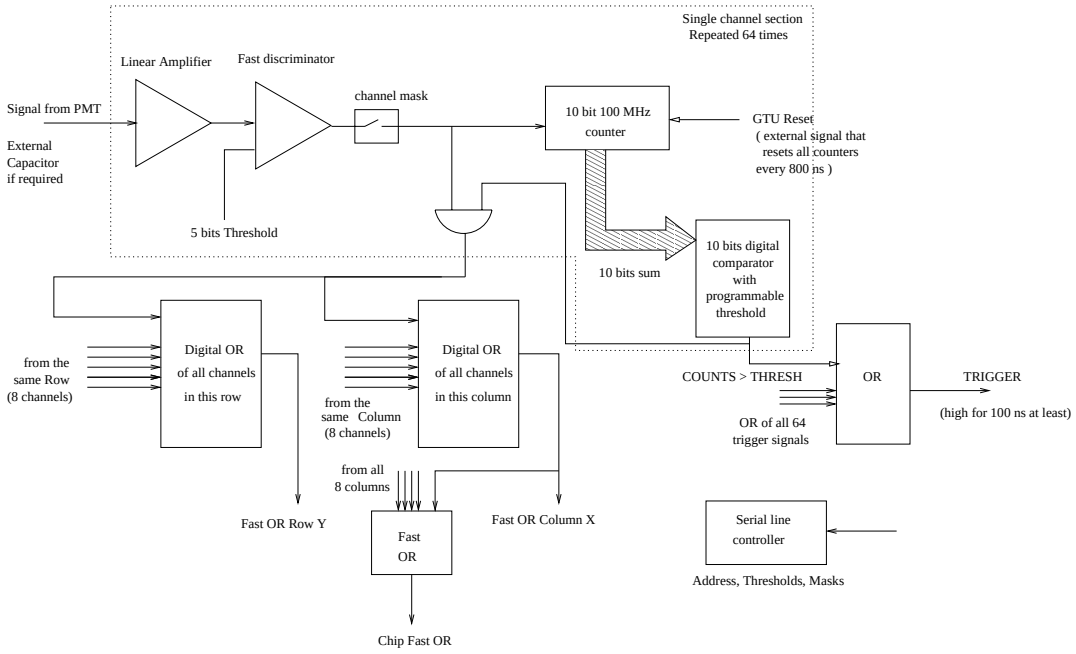

Figure 4.1: Basic block diagram of the very basic configuration of the chip. See the text for description.

In this configuration the chip is able to amplify and shape the analogue signal from the MAPMT, discriminate it with a programmable threshold, count the number of hits for each channel in a time window controlled by an external reset and provide fast-OR signals for rows, columns and the chip as a whole. It is expected to use time windows of about $800\ \mathrm{ns}$ corresponding to $1.25\ \mathrm{MHz}$.

A slow serial line is also required to be able to download parameters like thresholds and channel masks. Each chip must have an address to be able to handle many chips with a single serial line.

A total charge analogue output is also foreseen. It may be done either by amplifying and shaping the signal coming from the last dynode of the MAPMT or by summing the channels internally to the chip.

4.2.5 Technology and preliminary design

The chip design was started with the goals and guidelines described in the previous sections, following the basic block diagram depicted in figure 4.1.

A CMOS sub-micron technology was identified as the best candidate for this project fro the following reasons.

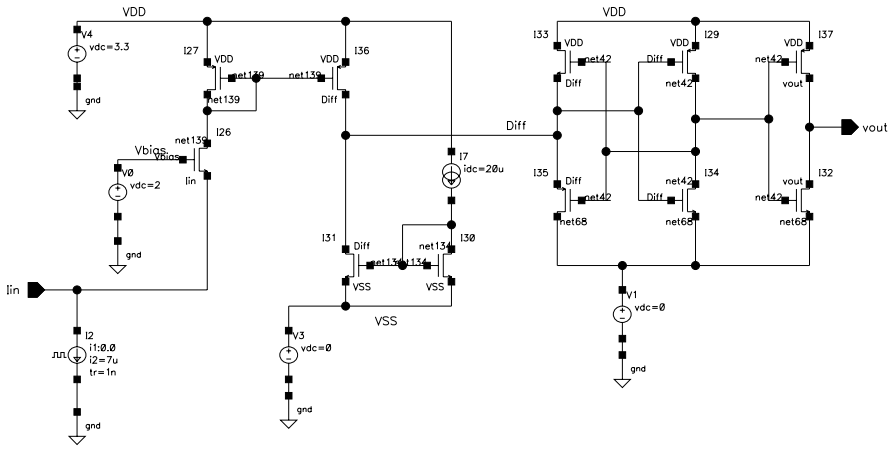

Figure 4.2: Preliminary design of a CMOS based front-end section, composed of a current preamplifier, a current threshold generator and a discriminator.

- It is widely available on the market.
- It is almost naturally radiation tolerant.
- It should give the possibility to get the required speed with very low power consumption.

The most critical part of this chip is obviously the front-end one (amplifier and discriminator). The other elements of the system are completely digital and run at $100\ \mathrm{MHz}$ maximum speed. It is already known, from existing and well tested devices, that digital functions at this (nowadays low) speed is not a problem.

Three slightly different current amplifiers and discriminators were identified. From preliminary simulations of these designs they look very promising, yielding to very large speed (one can get easily the $100\ \mathrm{MHz}$ bandwidth required) with very low power consumption.

The basic layout is depicted in figure 4.2. The simulated performance is shown in figure 4.3.

The simulation yields a total power consumption of about $0.3\ \mathrm{mW}$ in steady conditions (that is with no input signals), reaching a peak of $0.6\ \mathrm{mW}$ during transitions. With a background of about $1\ \mathrm{MHz}$ per channel the system as an active duty cycle below 1%, so the most important number is the first one, which is well within our goals.

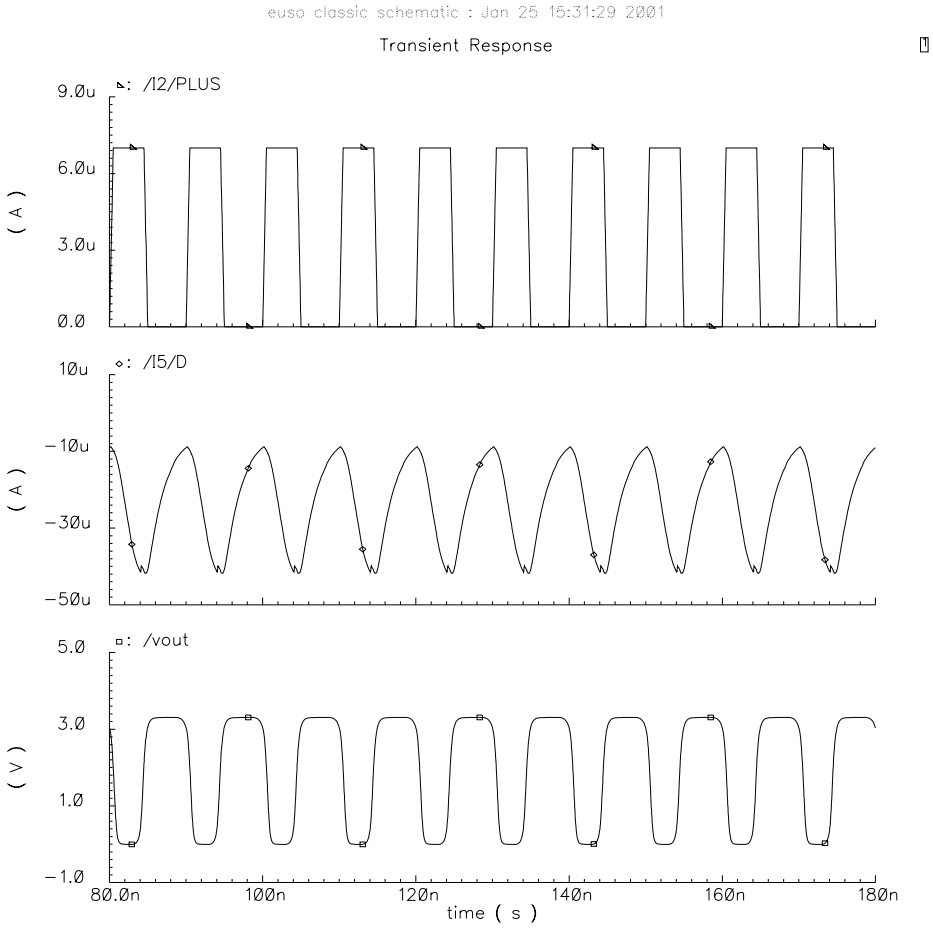

Figure 4.3: CAD simulation of the preliminary design shown in figure 4.2. The upper graph is the input current. The central one is the preamplifier output and the lower one is the discriminator output. It is clearly shown that $100\ \mathrm{MHz}$ is tolerable. The power consumption is about $0.3\ \mathrm{mW}$ in steady conditions and reach a peak of $0.6\ \mathrm{mW}$ during a single photon pulse.

Chapter 5

Focal surface engineering and integration

5.1 Focal surface design, construction and mechanical assembly

As the focal surface will be most probably curved, the packing of the devices has to be optimised to reduce losses in the geometrical acceptance, due to dead regions between the close packed devices, and defocusing effects, originating from a positioning of the sensor at some distance from the ideal focal surface. This makes the mechanical assembly difficult.

A curved focal surface requires a modular structure. The overall structure should consist of small functional units (*elementary cells*) assembled in super-modules. The elementary module consists of a limited number of MAPMT sharing some common resource like being installed on the same PCB base-board, having one common HV power supply and/or voltage divider, a common magnetic or electric screen (whenever required), common heat dissipation facilities and all of the front-end electronics plus as much as possible of the following readout electronics integrated in the module. This will correspond, physically, to the elementary unit described in section 5.3.1. In this report this will be called an *elementary cell*.

The elementary cells can be thick multi-layered Printed Circuit Boards (PCB), as described in section 5.3.1. A number of these modules, each one making an essentially autonomous system, are then put together to make a super-module. These are independent structures tied to each other by the support structure and having a shape determined by the layout of the focal surface.

5.2 Layout of the curved focal surface

The focal surface detector can be assembled by using a number of flat super-modules possibly using only a limited number of different shapes to reduce the design and construction complexity and to simplify the logic and structure of the trigger and readout electronics.

A few possible layouts have been studied. They are described in sections 5.2.1, 5.2.2 and 5.2.3. One more layout, based on square panels and optimising the filling in the central regions of the focal surface is under study. Its drawback is a more complex geometry.

5.2.1 Fitting by means of regular polyhedra

If the focal surface has a spherical shape the fit to the focal surface can be easily accomplished with a part of a polyhedron. The easiest way to accomplish this is to use a part of a Platonic polyhedron (in particular the Icosahedron or the Dodecahedron). In this case only one type of super-module will be required, having respectively, triangular or pentagonal shape. The dimensions of the modules are strictly determined by the radius of curvature of the surface and by geometry. In case the fit is not good enough one might attempt a better fit with a part of an Archimedean solid consisting of only two different shapes. One could use for instance the Truncated Icosahedron, consisting of identical hexagonal and pentagonal faces (the well known soccer ball), or the Icosidodecahedron, consisting of identical triangular and pentagonal faces. Others possibilities exist based on polyhedra with an even larger number of faces, which allow an even better approximation of a spherical surface, at the expense of increasing the number of super-modules and therefore the number of the edges, where some dead area will be unavoidably introduced. The drawback of this approach is that the super-modules (triangles, pentagons or hexagons) have to be filled with the sensors, the shape of which is invariably fixed to a square form, producing dead regions and requiring a complex geometry.

If the focal surface departs too much from the spherical shape, or in case the simple polyhedra described above do not provide a good enough fit, or in case the required triangular, pentagonal and hexagonal shapes required for the super-modules prove to be inconvenient, alternative geometries have to be conceived at the price to increase the number of different super-modules, as described below.

5.2.2 Fitting by means of trapezia

A general shape fitting any focal surface with cylindrical symmetry, including, as a particular case the sphere, might be built as follows by means of a segmentation in az-

imuth, producing spherical sectors (*lunes*). The surface is intersected with an appropriate number of planes passing by the axis of symmetry and forming equal angles between each other. The surface is then intersected with an appropriate number of planes orthogonal to the axis of symmetry, not necessarily at equal distances. The resulting regions determined in this way on the focal surface are then approximated by plane trapezia (the super-modules), except for the regions having one vertex at the vertex of the surface, having a triangular shape, which can be all removed and replaced by a single plane regular polygon perpendicular to the symmetry axis. The resulting focal surface is made of identical lunes, each one filled with variable shape and variable size elementary cells. A possible segmentation scheme based on this approach is shown in figure 5.1.

Some consequences and calculations deriving from this choice will be investigated in section 5.4.

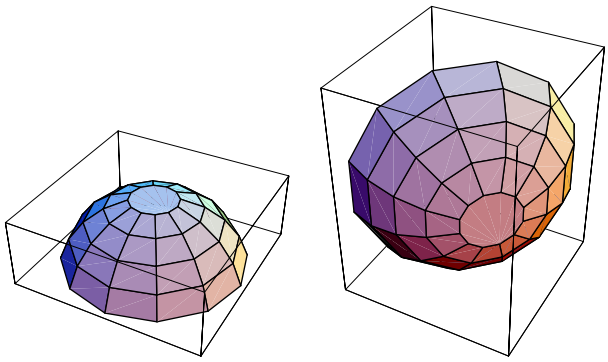

(a) Example One view (b) A second view

Figure 5.1: Two views of a focal surface layout based on a segmentation in azimuth.

5.2.3 Fitting by means of square panels

A second approach to fit any focal surface shape with cylindrical symmetry, including, as a particular case the sphere, can be built by a segmentation in polar angle, producing circular coronas. This arrangement can make use of square super-modules only, thus greatly simplifying the geometry, the logic and structure of the trigger and readout electronics. Assume to use square super-modules, made of $n \times n$ MAPMT, where good values for n might be $n = 6, 8, 10$ (to be optimised).

To tessellate, in an approximate way, the focal surface one might imagine to intersect the surface with an appropriate number of planes orthogonal to the axis of symmetry, not

at equal distances, but determining circles at equal polar angles which define circular coronae. The polar angles defining the different circles are determined by the dimensions of the square super-module. The resulting circular coronae determined in this way on the focal surface, strips running all the way round in azimuth, are then filled with closely packed square super-modules.

The advantage of this setup is the use of identical super-modules and the capability to obtain a good filling factor at the expense, probably, of a more complex mechanics, when compared to the option based on trapezia.

Note that the surface cannot be filled exactly with square shapes, but holes will unavoidably remain because a curved surface (a sphere, in particular) cannot be tessellated exactly by means of squares. This type of layout is shown in figure 5.2.3.

Some consequences and calculations deriving from this choice will be investigated in section 5.4.

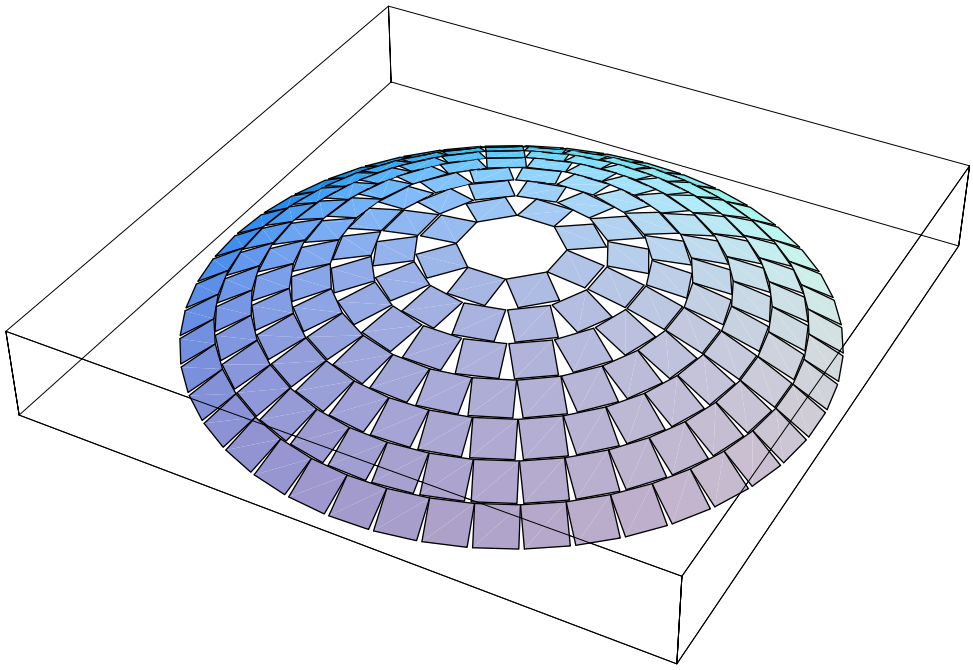

Figure 5.2: Focal surface layout based on a segmentation in polar angle and square super-modules.

5.2.4 Optimisation

The best solution has to be determined taking into account many requirements. The number of super-modules has to be optimised by taking into account the dead area between the super-modules (increasing with the number of super-modules), the need to have a good

fit to the focal surface (the required goodness of fit depends on the depth of focus of the optics and the fit becomes clearly better by increasing the number of super-modules) and the simplicity requirement to have a minimum number of different shapes to design and build. Finally the design has to match the architecture of the readout and trigger electronics.

5.3 MAPMT integration

The MAPMT base board and focal surface photo-detector have to be designed taking into account many constraints.

The dead space between the different modules has to be minimized. The heat produced by the MAPMT voltage divider and electronics has to be taken out. Any light leakage and any collection of stray light has to be avoided, including possible light entering the MAPMT from the backside. The HV requires careful insulation and to avoid discharges, requiring encapsulation and potting. The temperature has to be kept about constant at an appropriate value, to avoid thermal stresses and to operate in the most appropriate range of temperature for the MAPMT.

The engineering of the photo-detector surface has to take into account the large uncertainty on the MAPMT dimensions (up to 0.5 mm, according to the manufacturer). The large focal surface supporting structure has to withstand the effects of thermal expansion without compromising the MAPMT integrity.

The power supply system has to be carefully designed with respect to modularity, number of independent HV supplies and MAPMT grouping, in order to minimize cross-talk between MAPMT sharing the same HV supply or the same voltage divider and, in particular, to ensure that the probability that one unit is blind because one of the neighbouring units is seeing and intense source of background is reduced to an acceptable value.

5.3.1 MAPMT base-board

A prototype base-board was designed and prototyped for 2×2 MAPMT. This constitutes the elementary unit, with one single HV connection and one resistive bleeder circuit per MAPMT, to reduce the cross talk between the MAPMT compared to the case of one common resistive bleeder network. It was attempted to close-pack the MAPMT with a 26.7 mm pitch in the base design, leaving 1 mm between adjacent MAPMT. It was avoided to use any additional space along the edges of the board to allow close packing of different boards, again with 1 mm clearance. The heat produced by the bleeder circuit must be efficiently removed to avoid warm-up. This was accomplished by inserting a copper layer inside the PCB to be thermally connected to the cooling system. The board allows for mounting of the front-end chip on the same board as the voltage divider, on the

opposite side with respect to the MAPMT. In this way the front-end electronics is close to the photo-detector in a compact structure which minimize cabling.

The design of the base-board is shown in figure 5.3. Preliminary tests show that it is working as expected.

A view of the assembly of the elementary cell is shown in figure 5.4.

5.4 Tentative layout of the focal surface

Two tentative layouts of the focal surface were designed, one based on the scheme described in section 5.2.2 and another one based on the scheme described in section 5.2.3.

The focal surface dimensions are limited by the maximum dimensions allowed by the space mission and ISS environment, about $2.5\ \mathrm{m}$ diameter. This figure matches with the figures of table 1.4. The focal surface dimensions are therefore fixed by the obvious requirements to have as large as possible aperture and field of view of the optics. Note that the focal surface diameter is just equal to the optics diameter, D_M.

On the other hand the sensor dimensions are fixed, and these are the same for both the 64 channels version and the 16 channels version.

As the focal surface dimensions are fixed, and the same applies to the sensor and pixel size dimensions, the obvious requirement to fill as much as possible with sensors the focal surface unambiguously fixes the number of sensors and, as a consequence, the number of channels, once the number of channels per sensor has been chosen (unless one decides to use different MAPMT pixel sizes on different regions of the focal surface to match the PSF of the main optics). This then fixes the angular sensitivity of the instrument and the pixel size at the Earth surface.

As one will have identical pixels on the focal surface this implies that different pixels will see un-equal regions at Earth surface, depending on the pixel position.

A preliminary layout of the focal surface was designed based on this approach. This allows to determine the real number of sensors and channels and to compare them with the desired number of channels. This also allows to perform estimates of the mass and dimensions of the focal surface detector as well as estimates of the photo-detector efficiency and filling factor of the sensors on the focal surface.

Note that, assuming big enough super-modules, the fraction of EAS crossing the border between two super-modules is small. Therefore, when attempting naive estimates, it is more appropriate to include the effect of the filling factor on the focal surface on the rate of events that can be detected, and not on the efficiency for detecting a specific EAS.

At this stage no account is taken of the hole at the center of the structure present in both layouts which can certainly help the design of the mechanical structure of the photo-

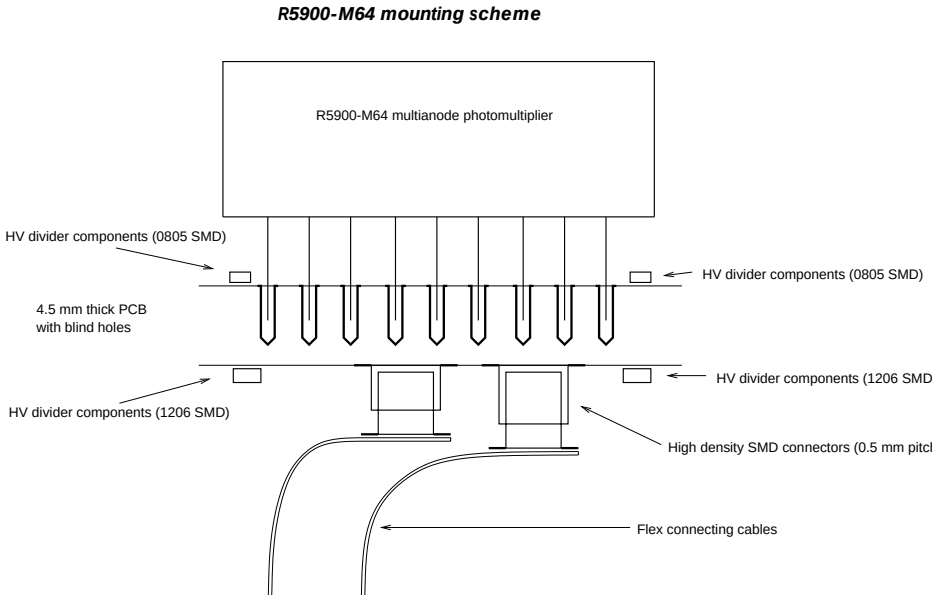

(a)

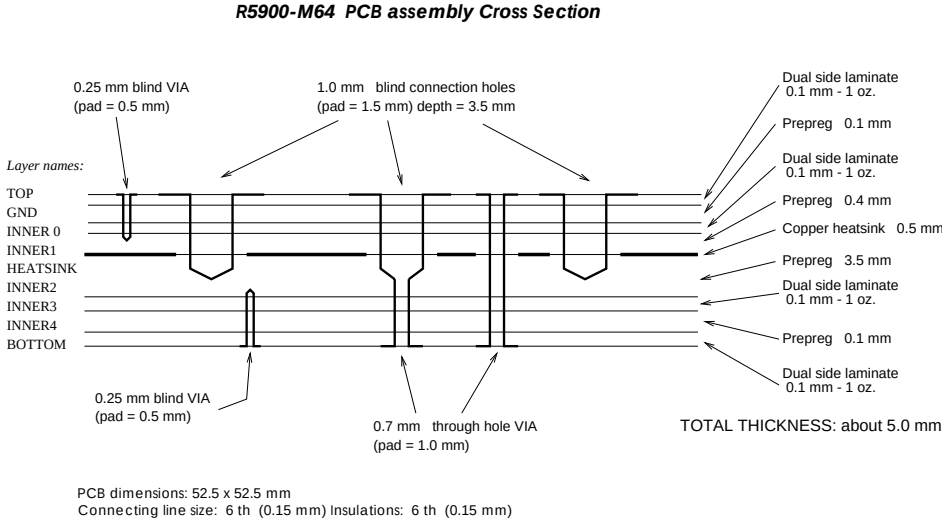

(b)

Figure 5.3: Mounting scheme and cross-sectional view of the elementary cell with four MAPMT. In the present prototype the signals are extracted by means of high-density connectors. In the final design the front-end chip will be installed on the back of the board.

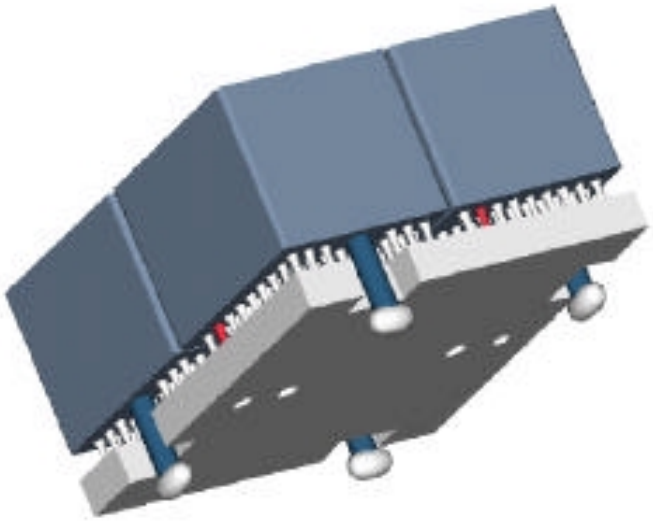

Figure 5.4: View of the elementary cell with one board housing four MAPMT.

detector and might house auxiliary instrumentation. Both schemes foresee a region which has the shape of a regular polygon on the axis. This region might be just forgotten or filled with a dedicated super-module. In any case the possible filling of this part with super-modules has to be designed in a specific fashion. Note however that the hole is only a small fraction of the total focal surface area.

In any case the PSF of the optics has to be optimised not on the axis (at zero field of view) but at some intermediate field angle, in such a way to optimise the overall average image quality on the focal surface (which also requires to take into account the transmission of the main optics).

5.4.1 Number of channels, sensors and super-modules

The desired number of pixels on Earth, assuming that every pixel will watch an area of $\approx 0.8 \times 0.8 \ \mathrm{km}^2$ on the Earth, can be calculated from 1.1: $N \simeq 2.36 \cdot 10^5$. Anyway the actual number of channels is determined by the real pixel dimension of the sensors and by the geometry of the focal surface layout. The number of MAPMT is only determined by the geometry of the focal surface and by the obvious requirement to put as many as possible MAPMT to fill the focal surface.

In what follows, in addition to the assumptions summarized in chapter 1, it is assumed that MAPMT can be closely packed in a rectangular array with $1 \ \mathrm{mm}$ space between each other. The resulting pitch will be therefore $p = 26.7 \ \mathrm{mm}$. Moreover the use of a light collector system, of the types described in chapter 3.2.1, will be assumed. What-

ever type of light collector system will be used it is assumed that it is capable to demagnify $26.7 \times 26.7\ \mathrm{mm}^2$ onto the $18.1 \times 18.1\ \mathrm{mm}^2$ of the MAPMT sensitive area, with a 1.48 demagnification factor. It is therefore assumed that the light collector system is capable to recover the $1\ \mathrm{mm}$ space left between adjacent MAPMT. In this way the resulting effective pixel size of the MAPMT turns out to be $d_{64} = 26.7/8 = 3.338\ \mathrm{mm}$ for the 64 channels (M64) version of the MAPMT and $d_{16} = 26.7/4 = 6.675\ \mathrm{mm}$ for the 16 channels (M16) version of the MAPMT.

The results are summarized in table 5.4.1.

	M16	M64
effective pixel size	$d_{16} = 6.675\ \mathrm{mm}$	$d_{64} = 3.338\ \mathrm{mm}$
effective pixel area	$d_{16}^2 = 44.5556\ \mathrm{mm}^2$	$d_{64}^2 = 11.1389\ \mathrm{mm}^2$
pixel angular aperture	$d\alpha = 2.67 \cdot 10^{-3}\ \mathrm{rad}$	$d\alpha = 1.34 \cdot 10^{-3}\ \mathrm{rad}$
pixel solid angle	$d\Omega = 7.13 \cdot 10^{-6}\ \mathrm{sr}$	$d\Omega = 1.78 \cdot 10^{-6}\ \mathrm{sr}$
pixel size on the Earth	$\Delta_E = 1.01\ \mathrm{km}$	$\Delta_E = 0.51\ \mathrm{km}$
maximum number of channels	$1.18 \cdot 10^5$	$4.72 \cdot 10^5$
maximum number of MAPMT	7384	7384

Table 5.1: The focal surface layout parameters.

The desired pixel size, $\delta = 4.72\ \mathrm{mm}$, therefore, lies in between the two possible real choices. This mismatch is unavoidable with the present input parameters. It might be fixed by tuning, if possible, some parameters such as the $f\#$ of the optics, if this were necessary.

The choice of the specific model of the sensor has therefore to be optimised taking into account the requirements from physics and the PSF of the optics. Different pixel sizes can also be used in different places, to match possible changes with position of the PSF.

Anyway, as the two versions of the MAPMT are physically equal (except for a different segmentation of the anode array) many conclusions can be drawn without considering the actual pixel size.

The choice of the type of MAPMT to use, M16 or M64, has to be optimised taking into account many things such as the requirements from Science, the PSF of the optics, the necessity to keep the number of readout channels close to the minimum required.

One possible option exploits the availability of different pixel sizes: as the PSF of the optics normally changes at different field angles one can use the different MAPMT pixel sizes in different regions of the focal surface.

5.4.2 Scheme based on squares

It will be assumed that each super-module is made of 6×6 MAPMT having, conservatively, a total dimension of $L = 170$ mm, which is more than 10 mm larger than the linear dimension of 6 close-packed MAPMT alone. This takes into account the space needed for the support of each super-module, heat dissipation facilities, thermal control devices, power supplies and electronics, cables and anything else is required.

As squares cannot tessellate exactly a spherical surface, a number of holes are left. Different schemes have been studied, the results are summarized in table 5.4.2. Note that the different schemes have slightly different angular coverage and therefore the number of MAPMT cannot be immediately compared among the different schemes. The filling factor is evaluated as the ratio between the area covered by the square super-modules and the total area of the spherical cap up to the maximum angle covered by the specific scheme. The geometrical acceptance is then evaluated as the product between the filling factor and the sensitive area inside each super-module, that is, with the present assumptions, about 0.89.

Note that the squares must be considered only as logical structures, while the real shape of the supporting module might be different, for instance a trapezium, to help the mechanical design. Moreover by a careful tuning of the different parameters one can arrange the layout to show an azimuthal segmentation (and therefore symmetry) given by the number of squares in the innermost corona, thus greatly simplifying the mechanics.

	Scheme 3	Scheme 4	Scheme 5	Scheme 6
Number of super-modules	154	159	166	173
Minimum angle	$2.3°$	$2.9°$	$3.4°$	$4.0°$
Maximum angle	$30.2°$	$30.8°$	$31.4°$	$32.0°$
Number of squares per corona	3/9/16/22/29/35/40	4/10/17/23/29/35/41	5/11/18/24/30/36/42	6/12/19/25/31/37/43
Filling factor	0.83	0.83	0.83	0.84
Number of MAPMT	5544	5724	5976	6228

Table 5.2: Focal surface layout parameters resulting from the scheme based on a segmentation in polar angle of the focal surface.

Note that the filling factor is approximately independent from the scheme but the angular coverage of the different schemes are different.

From the number of MAPMT in table 5.4.2 one can deduce the number of channels of the photo-detector, once defined the MAPMT type (M16 or M64). As the number of MAPMT, is of the order of $6 \cdot 10^3$ the resulting number of channels will range from $\approx 1 \cdot 10^5$ (when using only M16) to $\approx 4 \cdot 10^5$ (when using only M64).

A view of the layout resulting from the four schemes of table 5.4.2 is shown in figure 5.5.

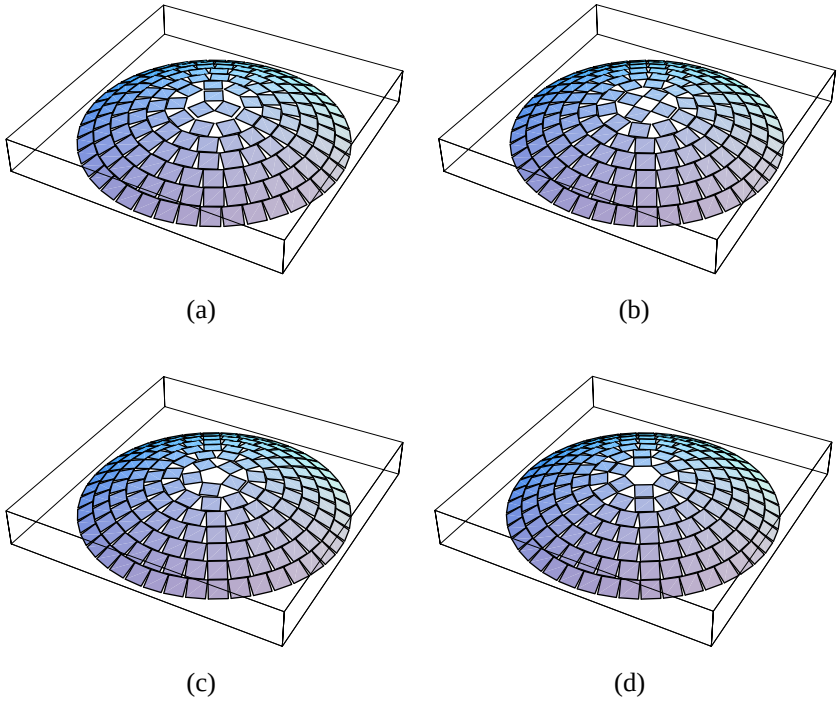

Figure 5.5: View of the four possible layouts corresponding to table 5.4.2.

An important point is the goodness of the fit of the super-modules to the exact focal surface. For a given radius of the focal surface, R, and side of a square, L, the maximum distance of a square from the sphere into which it is inscribed is at the square center. Therefore the sagitta has to be evaluated from the diagonal of the square, that is by $L\sqrt{2}$. The maximum distance is then given by the relation

$$d_R = R\left(1 - \sqrt{1 - L^2/(2R^2)}\right) \simeq L^2/(4R) \quad , \tag{5.1}$$

where the approximate relation applies when $L \ll R$. This relation gives, with the present data, a maximum distance of any square from the focal surface of about $3\ \mathrm{mm}$. This gives, by means of formula 1.10, a defocusing effect of $1.2\ \mathrm{mm}$. These figures can actually be reduced by about a factor two when one realizes that instead of inscribing the super-modules into the ideal focal surface one can inscribe them into a spherical surface with a radius larger by $d_R/2$, which provides an overall better fit to the ideal focal surface and reduces by a factor two the maximum distance from the focal surface. Note that when increasing

the side of the square the maximum discrepancy from the spherical surface rises quickly (as the square of the side).

5.4.3 Scheme based on trapezia

The focal surface is approximated with planar trapezia, inscribed into the ideal focal surface. A scheme was developed made of 24 identical sectors in azimuth each one made of seven plane trapezia.

The sectors are tied to each other by means of metallic structures running like the meridians of the surface. They hold the sectors in place, tie them to the external structure and might help to convey the heat to a convenient location for dissipation.

The detailed scheme of one sector is shown in figure 5.6. This results in 5808 MAPMT with a filling factor of 0.78 (with maximum angular coverage up to $30°$).

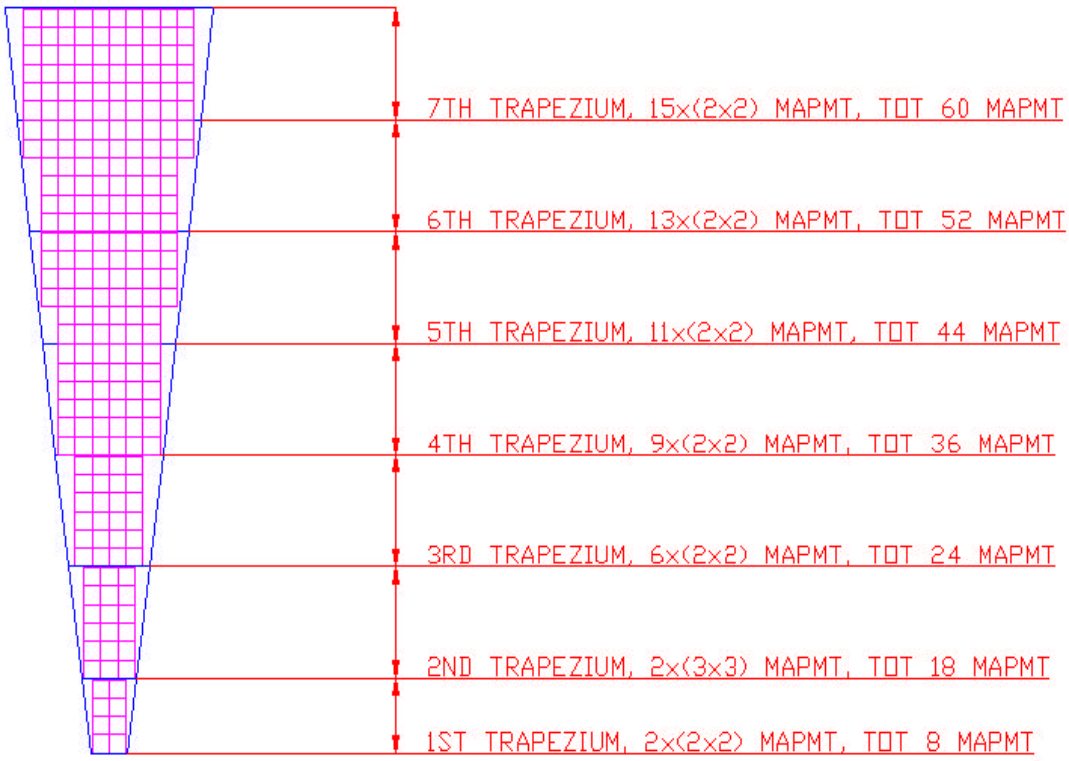

Figure 5.6: A possible segmentation scheme of the focal surface.

The maximum discrepancy is given in this case by the larger super-modules at the

outer edge and it results in ≈ 10 mm. As discussed in section 5.4.2 this figure can be actually reduced by a factor two by fitting the radial position of the super-modules to the ideal focal surface, instead of inscribing them into it.

5.4.3.1 Structural analysis of the structure

The structure has been analysed from the point of view of both static and dynamic loads. The aim of the study was to have a preliminary idea of the performance of the structure and to see whether the proposed solution was worth to be investigated in detail.

A finite element model has been built, with the following assumptions.

- Structure. The trapezia have been simulated as electronic boards, 6 mm thick, arranged in lunes. Trapezia and lunes are directly tied to the neighbouring ones, without any intermediate element (brackets and meridians). Such assumption greatly simplifies the model, but also increases its stiffness. The results can therefore be considered only as a preliminary indication.

- Constraints. Translations along the vertical direction (parallel to the axis of circular symmetry) have been set to zero for any node lying on the upper and lower edge. This is quite a relaxed scheme, adopted to compensate the effect of the model simplification described before. However, one can estimate that the constraints have a much larger influence than the stiffness increase.

- Loads. The structure has been submitted to its own weight, with the gravity acting along the axis of circular symmetry. For every element an added mass per unit of surface is included, that takes into account the mass of the systems housed on the element.

The static analysis (see figure 5.7) showed very little deflection: 0.067 mm (blue area), that become 0.091 mm with the mass of the light collector system. Similarly, the stress is very low, quite below the allowable value.

The dynamic analysis identified the first modal frequency at 62 Hz, neglecting at all any damping effect. During the launch, the structure will be submitted to an acceleration that is several times the natural gravity at sea level, and low frequency dynamic loads (mainly noise). Therefore a stiffer constraint scheme will be probably required to limit both stress and deformation and to displace to higher frequencies the first modal. Nevertheless, after these first results, the performance of the proposed structure looks promising.

5.4.4 Power and mass budgets

Very preliminary estimates of the mass and power budgets, based on the data in tables 1.4 and 1.4 were carried on.

5.4.4.1 Power budget

The power available to *EUSO* has to be shared with many other ISS systems. This sharing results in a considerable lack of any guarantee of power availability at any given level.

The limiting factor may also be the ability to dissipate energy at reasonable temperatures for external payloads such as *EUSO*.

The lack of guarantee of power availability at the observation time, the fact that the readout electronics has to be on only for a limited fraction of the orbital period ($\eta \approx 0.1 \div 0.2$) and the limited amount of power available point to the use of batteries acting as a power source for the readout electronics and as a buffer for any other system.

Very roughly one can assume to have an average power P_0 from the ISS and as a consequence an energy $P_0 T$ in the time T. If the power is only required for a fraction η of time (as it is the case for the readout electronics, but not for the MAPMT) one can in principle exploit, during the interval of time $T\eta$, a power P_0/η, neglecting the inefficiencies of the various steps. Given the short duty cycle ($\eta \approx 0.15$) the use of batteries can provide a significant increase of the effective power available to the readout electronics.

Suppose, very conservatively, that one needs, overall, $p_0 \simeq 5$ mW per channel for all the readout electronics, powered from $V \simeq 5$ V. With $4 \cdot 10^5$ channels, a conservative figure, one needs ≈ 2 kW, during a fraction η of time, which corresponds to drawing an average power of ≈ 0.3 kW from the ISS.

Batteries are routinely used in space experiments. $\mathrm{Ni-Cd}$ batteries for space applications can provide energy densities in the range of ≈ 40 W hour/ kg [29]. $\mathrm{Ni-H_2}$ batteries (which will be used on the ISS) can provide up to ≈ 60 W hour/ kg [29]. Future developments are foreseen ($\mathrm{Li-ion}$) with more than ≈ 100 W hour/ kg [29].

As discussed in section 3.2.4, it should be possible to keep the power consumption of the MAPMT below ≈ 200 W.

5.4.4.2 Mass budget

The photo-detector mass budget can be evaluated, very roughly, as follows. The mass of some items is very well known, while it is very difficult, at the present level of knowledge, to make a safe evaluation for many other items.

MAPMT	30 g
Lens (plastics)	$\approx$ 15 g
Base-board	8 g per MAPMT
Partial total	53 g per MAPMT

Table 5.3: Mass budget for the well-defined photo-detector items.

One has then to include other items such as the electronics components and chips, the connectors, the potting (but the volume to pot is small) and power supplies. The value of their mass is difficult to estimate at the present stage of knowledge. One can therefore try to be conservative and assume that the overall mass per MAPMT, including all the electronics and micro-cell structure, is 100 g per MAPMT, that is more than three times the mass of the bare MAPMT. The total mass of the photo-detector is then 600 kg, excluding the mechanical macro-structure.

Note that the mass is, to a first approximation, independent of the type of MAPMT used. In fact only a few of the items mentioned above depend on the number of channels (e.g. the connectors).

5.5 Active temperature control

An active temperature control is most probably required to keep by heating, during the night-time, the temperature reached during the day-time, avoiding thermal stresses on the large focal surface. Overheating outside the temperature range allowed by the MAPMT has to be avoided as well.

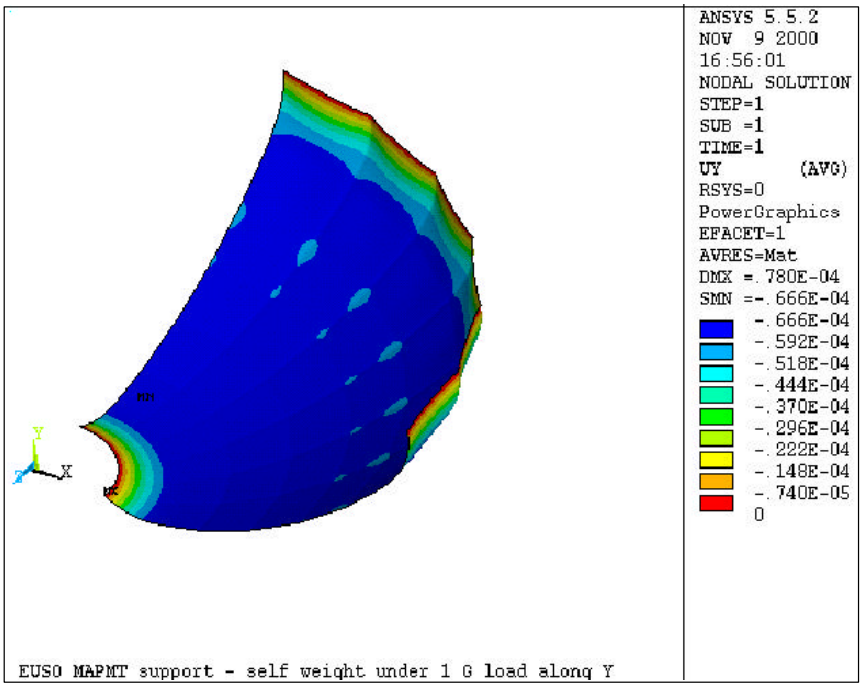

Figure 5.7: Static analysis of the focal surface layout.

Chapter 6

Activity plan

A preliminary R&D program has been carried out. A lot of work is necessary in order to reach a definitive design. There are problems to solve and technologies to push to the limit. Therefore a program of development, planning, optimisation and realization of the photo-detector (and the associate electronics) is required.

The main objectives of the phase A study will be the following.

- Precise definition of the characteristics and specifications required to a detector of EAS from the space.
- Development, optimisation and design of the photo-detector.
- Development and realization of the front-end electronics, definition of the possible solutions to interface the photo-detector with the trigger, read-out and system electronics.
- The realization and the test of functional prototypes, for the photo-detector qualification and to carry on important physical measurements (fluorescence yield, background, reflected Cherenkov light).
- Development of the appropriate calibration tools and methods for the photo-detector.

Work and tests on the critical issues are going on. Future work will include:

- optimisation and test of the light collector system;
- design and test of a voltage divider optimised for *EUSO*;
- design and realization of the elementary cell of the photo-detector and tests;

- space qualification tests of the MAPMT and the elementary cell;
- realization of a full, reduced-scale photo-detector element.
- optimisation and design of the focal surface layout;
- realization of a reduced size prototype, functionally equivalent to the EUSO photo-detector.

Acknowledgements

The authors want to thank Osvaldo Catalano and Piero Mazzinghi for many useful discussions and suggestions and Paolo Trampus for pointing out [29] as a source of information.

Chapter 7

The R5900/R7600 data-sheets.

In the following pages the data-sheets of the R5900/R7600 MAPMT are shown.

HAMAMATSU

PRELIMINARY DATA
JAN. 1999

MULTIANODE PHOTOMULTIPLIER TUBE ASSEMBLY H7546

FEATURES

- **8 × 8 Multianode**
- **Newly Developed "Metal Channel Dynode"**
- **High Speed Response**
- **Low Cross-talk**

GENERAL

Parameter		Description/Value	Unit
Spectral Response		300 to 650	nm
Wavelength of Maximum Response		420	nm
Photocathode	Material	Bialkali	—
	Minimum Effective Area	18.1 × 18.1	mm^2
Window Material		Borosilicate	—
Dynode	Structure	Metal Channel Dynode	—
	Number of Stages	12	—
Anode Size		2 × 2	mm^2
Weight		Approx. 30	g

MAXIMUM RATINGS (Absolute Maximum Values)

Parameter	Description/Value	Unit
Supply Voltage Between Anode and Cathode	1000	Vdc
Average Anode Current in total (at 800V)	0.018	mA

CHARACTERISTICS (at 25 °C)

Parameter		Value	Unit
Cathode Sensitivity	Luminous (2856K)	70	μA/lm
	Blue (CS 5-58 filter)	8	μA/lm-b
Quantum Efficiency at 390nm		20	%
Anode Sensitivity	Luminous (2856K)	21	A/lm
Gain		3.0×10^5	—
Anode Dark Current per Channel (after 30min. storage in darkness)		0.2	nA
Time Response (per Channel)	Anode Pulse Rise Time	1.5	ns
	Transit Time Spread (FWHM)	0.3	ns
Pulse Linearity per Channel (±5% Deviation)		0.6	mA
Cross-talk (with 1mm Optical Fiber)		2	%
Uniformity Among All Anodes		1: 3	—

NOTE: Anode characteristics are measured with the voltage distribution ratio shown below.

VOLTAGE DISTRIBUTION RATIO AND SUPPLY VOLTAGE

Electrodes	K	Dy1	Dy2	Dy3	Dy4	Dy5	···	Dy9	Dy10	Dy11	Dy12	P
Ratio	3	2	2	1	1	1 ··· 1		1	1	2	5	

Supply Voltage: 800Vdc, K: Cathode, Dy: Dynode, P: Anode

Figure 7.1:

Figure 1: Typical Spectral Response

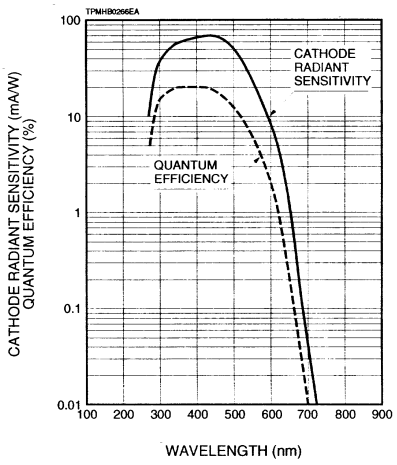

Figure 2: Typical Gain and Dark Current

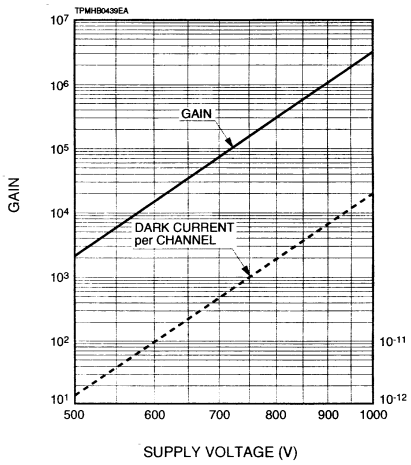

Figure 3: Typical Time Response

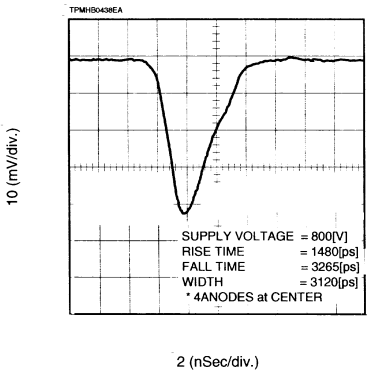

Figure 4: Typical Single Photoelectron PHD per Channel

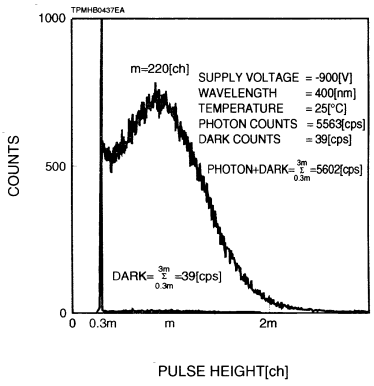

Figure 7.2:

Figure 5: Typical Anode Uniformity

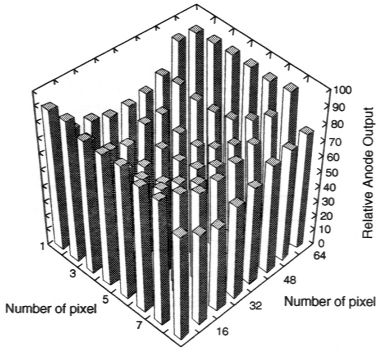

Each pole corresponds to each pixel of 64 anodes.
APPLIED VOLTAGE = 800 [V]
LIGHT SOURCE = W LAMP (DC LIGHT)
(Full Illumination on Photocathode.)

TPMHB0472EA

Figure 6: Anode Uniformity of One Pixcel

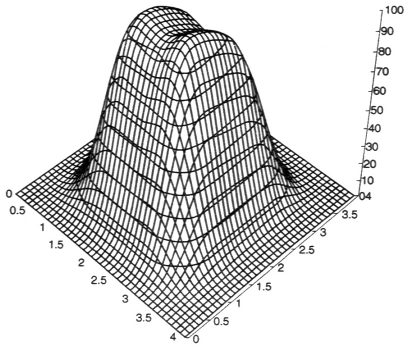

TPMHB0587EA

Figure 7: Anode Matrix

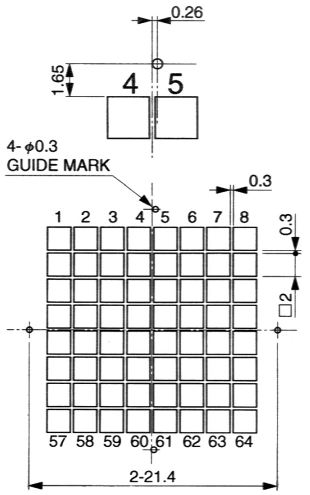

Anode Pattern
Top View

TPMHA0404EC

GUIDEMARK
(The center line of tube is not matched to the location of Guide Mark.)
The guide marks are holes of 0.3 mm in diameter on the electrode plate. They can be seen from top the R5900-00-M64 through its photocathode. As the guide marks are located nearly on the center line of 64 pixels, they can be used for positioning when scintillating or optical fibers are coupled to the R5900-00-M64.

Figure 7.3:

Figure 8: Dimensional Outline and Circuit Diagram (Unit: mm)

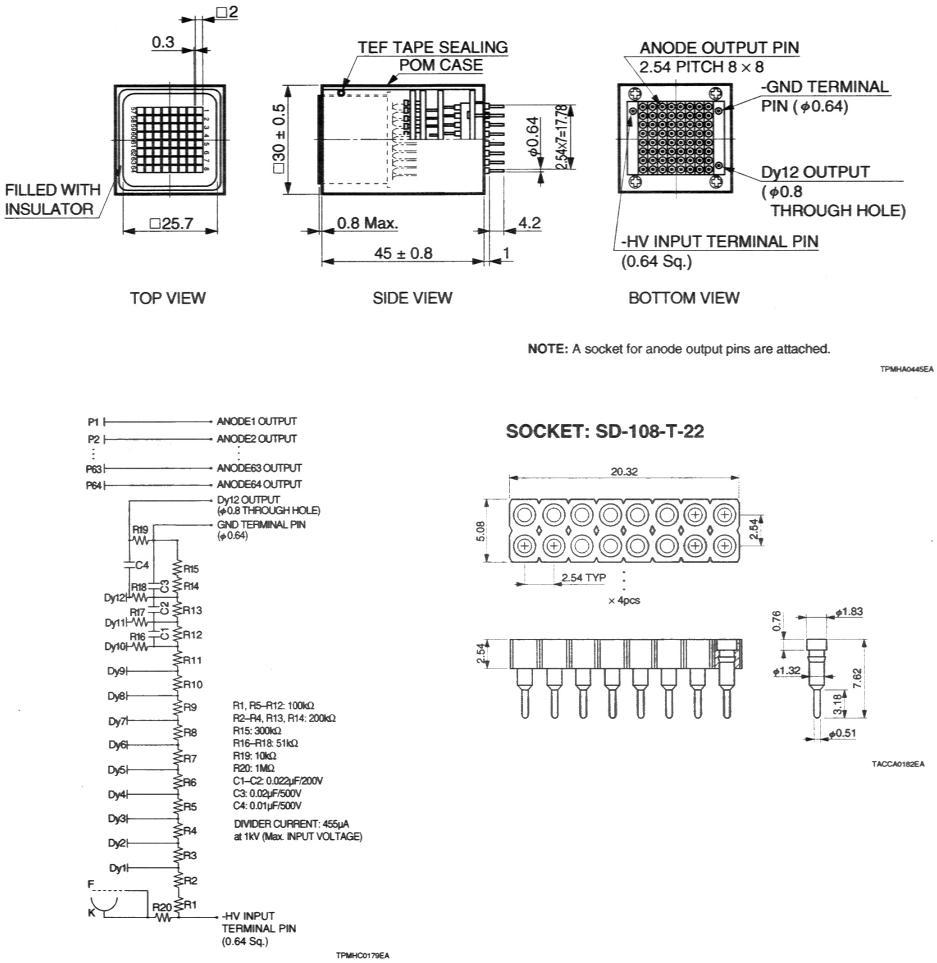

Figure 7.4:

Bibliography

[1] M. Ambriola et al., The AirWatch Collaboration, *Extreme energy cosmic rays (EECR) observation capabilities of an "AirWatch from space" mission*, Nucl. Phys. Proc. Suppl., 70 (1999) 515-517 .

[2] Osvaldo Catalano, *AirWatch from Space*, Progress Report, IFCAI-CNR Internal Note, Sep 24, 1999.

[3] O. Catalano et al., Proc. SPIE 3445, 478 (1998);
O. Catalano, Proc. 26 th ICRC 2, 407 (1999) and 2, 411 (1999).

[4] L. Scarsi et al., EUSO Collaboration, *EUSO - Extreme Universe Space Observatory*, Proposal for the ESA F2/F3 Mission, January 2000,
"http://www.ifcai.pa.cnr.it/EUSO/docs/EUSOproposal.pdf".
L. Scarsi et al., EUSO Collaboration, *EUSO: A Mission to Explore the Extremes of the Universe using the Highest Energy Cosmic Rays and Neutrinos*,
Report on the accommodation of EUSO on the Columbus Exposed Payload Facility, Submitted to ESA, ESA/MSM-GU/2000.462/AP/RDA, December 2000.

[5] Y. Takahashi, private communication.

[6] Hamamatsu Photonics K. K..

[7] The AirWatch Collaboration, *AirWatch: the fast detector*,
Workshop on Observing Giant Cosmic Ray Air Showers, College Park, MD, 13-15 November 1997, AIP Conf. Proc., 433, 353-357, (1998); J.F. Krizmanic, J.R. Ormes e R.E. Streitmatter editors, Woodbury.

[8] The AirWatch Collaboration, *AirWatch: the fast detector* ,
SPIE conference on EUV, X-ray and Gamma-ray Instrumentation for Astronomy, july 1998, San Diego, California, US, Proc. SPIE'98 Conf., 3445, 486-494, (1998).

[9] A. Petrolini, R.Stalio e A. Gregorio,
The OWL/AirWatch experiment: the focal plane detector ,
Proceedings of the 26th International Cosmic Ray Conference (ICRC 99), Salt Lake City, 17-25 august, 1999.
In Salt Lake City 1999, Cosmic ray, volume 2, 403-406, D. Kieda, M. Salamon and B. Dingus editors.

[10] V. Gibson, A. Petrolini et al., *Performance of a cluster of Multi-Anode Photomultipliers equipped with lenses for use in a prototype RICH detector*,
LHCb Internal Note 2000-083-RICH, 19th March 2001, to be submitted to NIM.

[11] T. Gys et al, Nucl. Instr. and Meth. A355 (1995) 386;
G. Anzivino et al., Nucl. Instr. and Meth. A365 (1995) 76;
R. DeSalvo, Nucl. Instr. and Meth. A387 (1997) 92;
E. Chesi et al., Nucl. Instr. and Meth. A387 (1997) 122.

[12] E. Albrecht et al., *Performance of hybrid photon detector prototypes with* 80% *active area for the RICH counters of LHCb*, Beaune'99, June 21-25, 1999, Nucl. Instr. and Meth. A442 (2000) 164.

[13] A. Braem et al., *Highly segmented large-area hybrid photodiodes with bialkali photocathodes and enclosed VLSI readout electronics*, Beaune'99, June 21-25, 1999, Nucl. Instr. and Meth. A442 (2000) 128.

[14] Flat Panels PMT, Hamamatsu Photonics K. K., private communication.

[15] Hamamatsu Photonics K. K., private communication.

[16] V. Gracco and A. Petrolini, *Use of multi-anode photomultipliers for the AirWatch photon detector*, 23 October 1998, AirWatch technical note,
"http://www.ge.infn.it/euso/docs/mapmt.ps"

[17] Multi-anode photomultiplier tube R5900/R7600, Hamamatsu Photonics K. K..

[18] R. Winston, J. Opt. Soc. Am., Vol. 60, No. 2, (1970) 245;
D. A. Harper et al., Appl. Opt., Vol. 15, No. 1 (1976) 53;
R. Winston and W. T. Welford, J. Opt. Soc. Am., Vol. 69, No. 4, (1979) 532;
R. Winston and W. T. Welford, J. Opt. Soc. Am., Vol. 69, No. 4, (1979) 536;
T. Jannson and R. Winston, J. Opt. Soc. Am. A, Vol. 3, No. 1, (1986) 7.

[19] W. J. Smith, *Modern optical engineering*, McGraw-Hill, 1966;
R. W. Ditchburn, *Light*, Academic Press, 1976.

[20] Precision Glass Products Company, Oreland, PA, USA.

[21] Katshushi Arisaka, UCLA, private communication.

[22] Schott Fiber Optics Inc., Southbridge, MA, USA.

[23] S. Cuneo et al., *A proposal for a supporting structure for the multianode photomultipliers of RICH2*,
LHCb Internal Note 2000-005-RICH, 19th February 2000.

[24] J. C. Zwinkels et al., Appl. Opt., Vol. 29, No. 22 (1990) 3240.

[25] Laser Focus World, 12/95.

[26] Geltech Inc., Orlando, Florida, USA.

[27] R. Forty, *Use of lenses to increase the RICH photodetector coverage*, LHCb note 98-038, 20/3/1998.

[28] R. Battiston, *Recent results from the Alpha Magnetic Spectrometer (AMS) on the STS-91*, astro-ph/0101547;
B. Alpat, AMS Collaboration, *Antimatter search with AMS (Alpha Magnetic Spectrometer) during STS-91 precursor flight*, Nucl. Phys. Proc. Suppl. 85, 15 (2000).

[29] Saft Alcatel Space, "`http://www.saft.alcatel.com/space/`".